Title

Clonal Dynamics in the Male Germline from Development to Next Generation

Authors

Tatsuro Ikeda[1,2,3*], Maurice Langhinrichs[2*], Tamar Nizharadze[2], Chieko Koike[1], Yuzuru Kato[4,5,6], Katsushi Yamaguchi[7], Shuji Shigenobu[4,7], Kana Yoshido[8], Shinnosuke Suzuki[1,4], Toshinori Nakagawa[1,4], Ayumi Maruyama[1], Seiya Mizuno[9], Satoru Takahashi[9], Hans-Reimer Rodewald[10], Thomas Höfer[2#], Shosei Yoshida[1,4#]

Affiliations

1. Division of Germ Cell Biology, National Institute for Basic Biology, National Institutes of Natural Sciences, Higashiyama 5-1, Myodaiji, Okazaki 444-8787, Japan
2. Division of Theoretical Systems Biology, German Cancer Research Center, Im Neuenheimer Feld 580, 69120 Heidelberg, Germany
3. Japan Society for the Promotion of Science, 5-3-1 Kojimachi, Chiyoda-ku, Tokyo 102-0083, Japan
4. Graduate Institute for Advanced Studies, SOKENDAI, Okazaki 444-8787, Japan
5. Department of Gene Function and Phenomics, Mammalian Development Laboratory, National Institute of Genetics, 1111 Mishima, Shizuoka 411-8582, Japan
6. Department of Genome Biology, Graduate School of Medicine, Osaka University, Yamadaoka 2-2, Suita 565-0871, Japan.
7. Trans-Omics Facility, National Institute for Basic Biology, National Institutes of Natural Sciences, Higashiyama 5-1, Myodaiji, Okazaki 444-8787, Japan
8. Laboratory of Theoretical Biology, Graduate School of Biostudies, Kyoto University, Yoshidakonoecho, Sakyo, Kyoto 606-8315, Japan.
9. Laboratory Animal Resource Center in Transborder Medical Research Center, University of Tsukuba 305-8575, Japan
10. Division of Cellular Immunology, German Cancer Research Center, Im Neuenheimer Feld 280, 69120 Heidelberg, Germany

* Equal contribution

\# Authors for correspondence: shosei@nibb.ac.jp, t.hoefer@dkfz-heidelberg.de

Abstract

Germ cells support the continuation and evolution of species. In mammals, the germline trajectory originates from a limited number of primordial germ cells (PGCs), persists through the lifespan of the organism, and continues across generations. Yet, the dynamics and contributions of individual PGC lineages remain enigmatic. Here, we employ *Polylox*[1] DNA barcoding to unveil the clonal dynamics of mouse male germline from development to the next generation and find that disparate probabilities for trans-generational inheritance from individual PGCs are established in early embryogenesis and persist throughout adulthood. Indeed, >30% of PCG clones are lost before colonisation in the testis, suggesting early quality control, with surviving PGC clones expanding unevenly. Thereafter, clone sizes remain stable lifelong, and inheritance to offspring is proportional to clone size, arguing against strong variability in sperm fitness. Mathematical analysis of the barcoding data indicates that early clonal dynamics follow probabilistic rules, whereas the subsequent compartmentalisation of clones into seminiferous tubules in the testis preserves the clonal repertoire and may guard against large-scale selection of mutant clones. This study defines the quantitative dynamics of male germline development and transmission and thus reveals constraints for how de novo mutations that arise in germ cells can be transmitted to offspring.

Main

The germline, distinct from the somatic lineage supporting bodily functions, is dedicated to generating gametes—sperm and eggs. Elucidating the clonal dynamics of germ cell lineage through an organism's lifespan and across generations is vital for understanding how heritable variations, including de novo mutations and epimutations that originate in the germline, are shaped through development and gametogenesis, and transmitted across generations. In mouse embryos, the germline is specified as a cluster of primordial germ cells (PGCs) in the posterior extraembryonic region around embryonic day (E)6.5. These cells then migrate through the hindgut to colonise the bilateral gonads by E10.5–11.5[1,2].

In male embryos, PGCs are directed towards the male fate and differentiate into gonocytes (or prospermatogonia) within the testis microenvironment, followed by compartmentalisation into approximately 10–11 separate seminiferous tubules formed by somatic Sertoli cells[3] (designated as testis cords before postnatal lumenisation). Gonocytes proliferate mitotically until around E14.5, after which they enter cell cycle arrest until birth[4,5]. Following birth, gonocytes resume proliferation, and a subset establishes the self-renewing pool of spermatogonial stem cells (SSCs) that sustain sperm production throughout life[6]. Although these steps of germline development have been well characterised at the population level, the clonal dynamics of individual PGC lineages, as well as the underlying rules and mechanisms, remain poorly understood.

Previously, clonal fates of the germline have been studied using multiple lineage-tracing methods at sparse resolution. Classically, labelling with lysinated rhodamine dextran (LRDX) revealed that a fraction of cells within E6.0–6.5 mouse embryos contribute to both PGCs and extraembryonic tissues[7]. More recently, strategies such as ES cell chimeras and Cre/loxP-mediated recombination, relying on one or a few fluorescent proteins, have been employed to study PGC clonal behaviours[8-10]. These studies revealed heterogeneous patterns of proliferation, localisation, and cell death across developmental stages. However, the limited number of markers in these studies restricts the ability to distinguish the tens to thousands of clones and did not allow to track clones continuously into adulthood and the next generation.

To overcome this limitation, considerable efforts have been devoted to DNA barcoding methods, which enable the individual labelling of large numbers of cells by introducing highly diverse genomic sequences[11-19]. Several reported barcoding strategies rely on CRISPR/Cas9 editing, where the distinction between "clonal" barcodes—those generated uniquely within a single cell—and "common" ones that have higher probabilities of arising independently in

83 multiple cells remains difficult to achieve. By contrast, the *Polylox* technology[12] can generate
84 DNA barcodes in specific cell populations in vivo through Cre/loxP-mediated recombination, and,
85 by knowledge of the recombination mechanism, allows the estimation of each barcode's
86 generation probability (P_{gen}) and thus the identification of clonal barcodes. Here, by applying
87 *Polylox*, we barcoded the whole population of mouse male PGCs and tracked their clonal
88 dynamics through development into the next generation.
89

90 **Tracing the PGC-clonal repertoire through development and adulthood**

91 To barcode embryonic PGCs using *Polylox*, we developed a *Prdm14-Mer-iCre-Mer* (*MiCM*)
92 transgenic mouse line, which expresses MiCM, a strictly tamoxifen-dependent Cre
93 recombinase[20,21] under the control of the *Prdm14* regulatory region (Extended Data Fig. 1a,b).
94 *Prdm14* is essential for PGC specification and germline establishment, showing specific
95 expression in PGCs from E6.5 to E14.5[22]. We crossed male and female mice harbouring *Prdm14-*
96 *MiCM* and *Polylox*, respectively, to obtain double-transgenic embryos (Fig. 1a, Supplementary
97 Table 1). By injecting 4-hydroxytamoxifen (4-OHT) into pregnant females, barcodes were
98 generated exclusively in the embryos' PGCs but not in gonadal somatic cells in a strict 4-OHT
99 dependent manner (Extended Data Fig. 1c–e, Supplementary Fig. 1a), without affecting the
100 distribution and number of PGCs (Extended Data Fig. 1f,g, Supplementary Table 2).
101 Using this experimental setting, we first analysed the clonal dynamics of the initially
102 established PGCs (Fig. 1a). Following consecutive 4-OHT injections at E6.5 and E6.75 (hereafter
103 collectively referred to as E6.5), tissues including all germ cells, namely the posterior half of the
104 embryo including the allantois at E8.5 and the bilateral testes from E12.5 through 1 year after
105 birth, were collected from multiple male mice. To comprehensively catalogue germline barcodes
106 in these samples, we performed long-read amplicon sequencing of the *Polylox* locus at high
107 sequencing depth (Fig. 1a, Extended Data Fig. 2a).
108 At E8.5, we detected 58.2 ± 13.8 (SD) barcodes per individual (N=6 mice) (Fig. 1b,c,
109 Supplementary Table 3). Notably, barcode diversity does not directly reflect the number of PGC
110 clones, since some common barcodes are expected to have arisen independently in multiple
111 PGCs[12], whereas clonal barcodes will have been generated in a single PGC only. Therefore, by
112 simulating barcode generation as random sequences of *Polylox* recombination[12], we estimated
113 that the recovered barcode repertoire at E8.5 corresponded to 126.2 ± 35.2 clones (Extended Data
114 Fig. 2b; Supplementary Methods), in close agreement with the reported count of PGCs[23].
115 Interestingly, the recovered barcodes decreased to 24.5 ± 7.6 at E12.5 (left and right testes

116 combined, N=13 mice) (Fig. 1b,c, Supplementary Table 4). Thereafter, the barcode count
117 remained stable from late embryonic development through one year after birth (Fig. 1c,
118 Supplementary Fig. 1a, Supplementary Table 4,5). This initial decline highlights a marked
119 reduction in clonal diversity, in which E6.5-labeled PGC clones undergo substantial "pruning"
120 during migration to the embryonic gonads. Once settled in the testes, such PGC clones persist
121 through germline development into adulthood.

122 Next, we analysed the PGC clone size, i.e., the number of constituent cells. First, we
123 verified that the barcode read frequency is proportional to the number of cells carrying each
124 barcode (Extended Data Fig. 2c, Supplementary Fig. 1b, Supplementary Table 3,5). We then
125 focused on clonal barcodes, whose calculated small generation probability ($P_{gen} < 0.001$) suggests
126 their generation within a single PGC. We found that the contribution of each clonal barcode
127 recovered at E8.5 was largely even, around 1% of all barcode reads (Fig. 1d), consistent with the
128 observation that a single mouse embryo contains 116 ± 4.4 PGCs at this stage[23]. However, by
129 E12.5, when ~3,500 PGCs are found in bilateral testes (Extended Data Fig. 1f), the distribution
130 of clonal barcode contribution became uneven, ranging from less than 1% (<35 cells per clone)
131 to about 10% of the total barcode reads (i.e., about 350 cells per clone) (Fig. 1d, Extended Data
132 Fig. 2d). While the total germ cell number increased substantially after E12.5, the uneven clonal
133 contributions remained largely stable into adulthood.

134 Approximately half of clonal barcodes were shared between bilateral testes at E12.5
135 and beyond, while the remaining half were restricted to one side (Extended data Fig. 2e,f). Clonal
136 barcodes observed bilaterally showed greater read frequencies, indicating larger clone sizes, than
137 those detected unilaterally (Extended data Fig. 2g). These results indicate that the variation in
138 clone size arises during PGC migration, before they split to colonise the bilateral testes.

139

140 **Clone size-dependent transmission to the offspring**

141 To assess how the uneven contributions of E6.5 PGC-derived clones are propagated through SSCs,
142 spermatogenesis, and into the next generation, four E6.5-barcoded males were mated with
143 multiple females from 2 to 10 months of age (Fig. 2a). At one year, the males were sacrificed, and
144 barcodes were analysed in FACS-sorted SSC pool and in whole testes, representing bulk
145 spermatogenesis (Supplementary Fig. 1b, Supplementary Table 4). We also analysed the barcodes
146 transmitted to offspring. Since the fathers were heterozygous for *Polylox*, approximately half of
147 the >200 offspring sired by each male inherited barcodes. Sanger sequencing of the offspring's
148 *Polylox* loci revealed ~20 barcodes transmitted from each father (Supplementary Table 6).

We found that clone compositions showed strong concordance between SSCs, the whole testis, and the offspring (Fig. 2b,c, Extended Data Fig. 3a–e). Barcodes with major contributions to SSCs and spermatogenesis were frequently found in offspring, whereas those with minor contributions appeared only infrequently or never. Together, the clonal compositions of E6.5-PGC derived SSCs in fathers are faithfully mirrored in spermatogenesis and transmitted to the next generation.

We then asked whether the PGC clones' contribution to spermatogenesis, and hence their transmission to the next generation, drifts over the course of paternal ageing (Extended Data Fig. 3f). However, the barcodes observed in offspring showed no signature of paternal age-dependence, a conclusion further supported by statistical analyses (Extended Data Fig. 3g,h). Therefore, once the SSC pool is established, early PGC-derived clones contribute stably and proportionally to spermatogenesis throughout the reproductive lifespan.

Combining the observed pruning during embryonic development and subsequent lifelong preservation of clonal divergence, we conclude that the early dynamics of PGCs shape their long-term outcome in their contribution to sperm and the next generation.

Stochastic dynamics of PGC clones and prediction of a "non-arriving" fraction

Given the decisive impact of early clone pruning on long-term spermatogenesis and transgenerational inheritance, we conducted mathematical analyses to gain insights into the rules and mechanisms of this process. We first asked which scenario is best supported by the barcoding data: (i) PGC fate is predetermined for survival or loss, (ii) PGCs follow stochastic dynamics shaped by variable selective advantages, or (iii) PGCs form a functionally uniform population governed by neutral stochastic dynamics.

We found that, when rescaling all clone sizes (Fig. 1d) by the mean clone size, the cumulative distribution of scaled clone sizes x is exponential, e^{-x}, at E8.5 and all subsequent time points, as well as in the next generations (Extended Data Fig. 4a,b). Such a shape-invariant exponential distribution of mean-normalized clone sizes is a robust indicator of a neutral drift "birth-death" process, in which cells undergo stochastic division ("birth") and loss ("death") (Supplementary Methods). By contrast, if a subset of PGC clones expanded under heritable and non-neutral selective advantages, the clone-size distribution would deviate from exponentiality, developing a heavier tail (Extended Data Fig. 4c,d). These analyses provide strong support for scenario (iii): PGC fates are governed by neutral probabilistic dynamics, with minimal, if any, contribution from heritable selective advantages.

Motivated by the implication that PGCs follow neutral stochastic dynamics, we next sought to mathematically resolve their behaviour across formation, proliferation, and migration to bilateral gonads. To this end, we modelled four plausible schemes based on stochastic birth-death processes of PGCs and the generation of *Polylox* barcodes through multiple recombination events. Using Bayesian inference, we then evaluated the predictive capacity of each model against the experimental data, including the identity and composition of measured barcodes, the degree of barcode sharing between bilateral testes, and the overall kinetics of PGC numbers between E6.5 and E12.5[23,24] (Extended Data Fig. 5a,b; Supplementary Methods). The model simulations revealed a remarkably high predictive ability if PGCs are assumed to all survive during migration but a fraction of them do not reach the testes (Model 1; Fig. 3a,b and Extended Data Fig. 5a–f). Such cell loss during migration was modelled as a stochastic transition to a "non-arriving PGC" fraction, in which cells are still present at least until E9.5 but will not be involved in the testis at E12.5 or contribute to subsequent, definitive germline. None of the other three models (Models 2–4) explained the measurements with realistic parameters and were therefore discarded (Extended Data Fig. 5a). Thus, Model 1 explains the measured data and makes a testable prediction of the "non-arriving PGC" fraction.

The high predictive capacity of Model 1 enabled us to simulate the clone dynamics of PGCs and to infer their key quantitative properties (Fig. 3c). During early migration phase, when PGC clones consist of only a few cells, stochastic cell division and loss introduce random variations in clone size, estimated to range from one to >12 cells per clone at ~E9.5. This heterogeneity in clone size becomes proportionally fixed during the subsequent expansion phase, as the influence of random division and loss diminishes with increasing clone size, leading to stable PGC contributions by ~E11 (Fig. 3c bottom). It is also estimated that, among the initial PGCs observed at E6.5, ~68% contribute to the definitive germline, with ~71% contributing bilaterally and ~29% unilaterally to the testes (Extended Data Fig. 5g,h). Further, larger clones at E9.5 are expected more to contribute bilaterally and to be kept still large till E12.5 (Extended Data Fig. 5h,i), indeed consistent with the observed relationship between clonal frequency and bilaterality (Extended data Fig. 2g).

Identification and characterisation of the predicted non-arriving PGC fraction

Our modelling analysis predicts that a significant fraction of PGCs become "non-arriving", failing to settle in the testis and hence not contributing to the definitive germline. We addressed this prediction and investigated the cellular identity of "non-arriving" cells. One possibility is that,

while initiating the PGC programme, some cells may ultimately differentiate into somatic lineages. This scenario is consistent with previous studies of *Blimp1*- and *Dppa3*-expressing cells, based on co-immunostaining, transplantation, and Cre-driven reporter analyses[25,26]. Previous in toto imaging of mouse embryos has also revealed that a subset of PGCs migrate into the extraembryonic region[27]. Furthermore, some PGCs may fail to reach the gonads by E10.5 and are eventually eliminated, as reported previously[28,29].

In our experimental system, to characterize the cells that had expressed *Prdm14* at E6.5 in vivo, we labelled them with GFP using *CAG-CAT-EGFP* reporter[30], instead of *Polylox* to allow for microscopy readout (Fig. 3d, Supplementary Table 7). Following 4-OHT injection at E6.5, we observed GFP-labelled cells exclusively within an extraembryonic region adjacent to the posterior tip of the epiblast at E7.5 (Fig. 3e), consistent with the reported PRDM14 expression at this stage[22]. We found that some GFP-positive cells were negative for OCT4, another marker of PGCs (Fig. 3e, Extended Data Fig. 5j). Notably, at E8.5, ~52% (125/239) of GFP^+ cells were $OCT4^+$ and located anteriorly near the hindgut, while the other ~48% (114/239) were $OCT4^-$ and located posteriorly on the allantois (Fig. 3f, Extended Data Fig. 5j). Within the GFP^+OCT4^- cells, ~69% (36/52) expressed extraembryonic mesoderm marker FOXF1[31] (Extended Data Fig. 5k).

Our barcoding experiments reveal that, among the descendants of *Prdm14*$^+$ presumptive PGCs at E6.5, only about half establish the definitive germline, whereas the remainder adopt a different fate. This is consistent with the view that PGCs commit to the germline only after colonising the gonads, under the influence of gonadal signals and DAZL expression[32-34]. In line with this, recent single-cell analyses indicate that *Prdm14*$^+$ cells constitute common precursors of PGCs and extraembryonic mesoderm, whose PGC potential becomes progressively restricted as their BMP responsiveness increases[35]. Together, these complementary findings converge on a coherent model in which a subset of *Prdm14*$^+$ cells establish the definitive germline by activating a core set of germline-identity genes (including *Prdm14*, *Oct4*, *Blimp1*, *Tcfap2c*, and *Dppa3*)[2], as they migrate into the embryonic gonads.

From the perspective of clonal dynamics, such refinement of PGCs results in significant loss and unequal expansion of testis-colonising clones. We speculate that such selective processes during this early phase may play a role in establishing the integrity of germ cell population for their future production of functional gametes.

Turnover of gonocyte sub-clones within parental PGC clones

Having observed a marked stabilisation of PGC clone dynamics in later stages, we next turned to

248 this slower clonal evolution. As described, after colonisation in the testis, the composition of E6.5-
249 labeled PGC clones remained stable from the late embryogenesis through postnatal and adult
250 stages, with individual clone sizes increasing in parallel with the overall germ cell population[31].
251 However, while these "parental clones" persisted, it remained unknown whether the constituent
252 "sub-clones" were proportionally maintained or instead subject to loss and expansion.

253 To address this question, we barcoded the gonocytes at E11.5 and analysed the
254 composition of recovered barcodes at subsequent time points (Fig. 4a, Supplementary Table 8).
255 The barcode number decreased from E12.5 (416 ± 171 per individual) to 1 week after birth,
256 around which SSCs are established (242 ± 50) (Fig. 4b). Following this period, the number of
257 recovered barcodes remained stable until 1 year old. Focusing on clonal barcodes ($P_{gen} < 0.00003$;
258 indicating single gonocyte-derived sub-clones), we estimated that the fraction of sub-clones
259 surviving from embryonic to adult stages is ~50% (Extended Data Fig. 6). Further, at E12.5 and
260 E13.5, contributions of individual clonal barcodes were relatively even around 0.03%, which
261 became diverged by 1 week after birth and maintained until one year old (Fig. 4c).

262 These findings indicate that, in contrast to the high stability of the "parental" PGC
263 clones, their "sub-clones" undergo loss and expansion during the late embryonic and perinatal
264 periods. Interestingly, although the E11.5-labelled sub-clones became stable during adulthood, it
265 is established that adult SSC-derived clones (i.e., "sub-sub-clones") also undergo loss and
266 replacement during homeostasis[36,37]. This highlights a hierarchical mode of clonal dynamics, in
267 which stabilisation occurs at large scale, while continual turnover persists at small scale.
268

269 **Segregated spatial distribution of PGC clones in seminiferous tubules**

270 PGCs migrate through embryonic tissues and settle in the testes as a sparse population. Across
271 this translocation into the testis, germ cells experience a drastic change in tissue architecture,
272 which could underlie the stabilisation of clone dynamics. By E13.5, PGCs are incorporated into
273 ~11 distinct testis cords (Extended Data Fig. 1g). Testis cords develop into seminiferous tubules
274 through postnatal lumenisation, ultimately extending up to 2 meters in total length per testis in
275 adults[3,38,39]. Through this process, germ cells are confined within a distinct, quasi-one-
276 dimensional tubular geometry, which may restrict clonal intermixing.

277 To gain insight into the functional relevance of such compartmentalisation, we
278 examined the spatial distribution of germline clones within seminiferous tubules. Following
279 barcoding at E6.5, all seminiferous tubules from two testes, each derived from different adult
280 male mice, were collected in fragments ranging from 1 to 13 cm in length (Fig. 4d, Supplementary

Table 9,10). Strikingly, tubule fragments, whether long (~10 cm) or short (<4 cm), contained only a minor subset of the collective barcode repertoire, typically 2–7 barcodes (Fig. 4e, Extended Data Fig. 7a–c). Furthermore, sub-fragments cut from longer fragments tended to share a common set of barcodes (Extended Data Fig. 7d). These findings suggest limited clonal intermixing within seminiferous tubules.

Modelling the germline clone behaviour through development and homeostasis

Then, to quantitatively capture how PGC clones behave within seminiferous tubules, we extended our previous model into adulthood by incorporating the tubular anatomical configuration (Fig. 5a, Extended Data Fig. 8). In this scheme, at E12.5, germ cells were segregated and aligned within a one-dimensional arrangement of ~11 seminiferous tubules, which elongated unevenly[38] until 2 weeks after birth when Sertoli cells ceased proliferation[40,41] (Extended Data Fig. 8d, Supplementary Table 11). SSC population expanded in proportion to the tubule elongation till this stage and then remained constant. We also incorporated the observed ~50% loss of the E11.5-labeled PGC sub-clones (Extended Data Fig. 6) and the previously reported stochastic neighbour turnover of SSCs during homeostatis[37] (Supplementary Methods).

In this modelling scheme, we found that the spatial arrangement of the clones in later stages was strongly influenced by their distribution upon their compartmentalisation into testis cords at E12.5. To guide our experiments, we modelled computationally a range of plausible spatial arrangements—from complete mixing to various local patch structures—and then compared the simulated and observed barcode distributions in long and short fragments of adult seminiferous tubules (Fig. 4e, Extended Data Fig. 7, 8a–c). The observed limited barcode diversity in long fragments indicates that individual PGC clones showed restricted contribution to only a subset of the eleven seminiferous tubule loops. However, intriguingly, a simple contiguous allocation of each clone within a single tubule does not explain the comparable barcode numbers included in short and long fragments. Instead, our modelling infers a locally repetitive patch structure, where alternating PGC clones form small patches containing ~150 SSCs on average, capturing all key experimental observations (Fig. 5b, Extended Data Fig. 8a,b,d,e).

To experimentally assess the model-predicted clone distribution patterns, we visualized E6.5 PGC clones 4-5 weeks after birth, using *Confetti*, a multi-colour fluorescent protein reporter[42], instead of *Polylox* (Fig. 5c top). With very low recombination efficiencies, coloured germ cells were detected in the testes of 5 out of 9 mice, 3 of which showed only a single

colour (Extended Data Fig. 9a), suggesting that cells marked by the same colour belong to a single, or very few, PGC clones. In these samples, cells of a particular colour formed clustered patches separated by unlabelled cells, confined to restricted regions within a limited subset of seminiferous tubules (Fig. 5c, Extended Data Fig. 9b,c). This spatial pattern aligns well with the model prediction, supporting a locally repetitive clonal patch structure achieved during testis development.

Tubular geometry and population effects stabilise the germline clonal dynamics

Our model reflecting the seminiferous tubule geometry stably maintained germ cell clones over extended periods. Extrapolation to 2 years predicted only minimal changes in clone numbers and patch-length distributions (Extended Data Fig. 10a,b). Therefore, we considered how such stabilisation occurs after compartmentalisation into seminiferous tubules. First, a *population effect* is likely to contribute: clone size itself buffers stability, with early small clones readily going extinct, whereas later enlarged clones persisting stably. In addition, a *geometric effect* may arise from the 1D arrangement: with clones occupying continuous stretches, only rare loss–replacement events that occur at boundaries between neighbouring clones can influence clone size evolution, while the majority of turnover that occurs intraclonally, within a clonal patch, does not.

We evaluated the role of the geometric effect by comparing simulated clone dynamics in models with different geometries. In addition to a truly one-dimensional (1D) model, we implemented a quasi-one-dimensional (q-1D) model[36] reflecting the cylindrical architecture of tubules, and a global competition model, in which any SSC can compensate for loss of another SSC regardless of their relative positions (Fig. 5d; Extended Data Fig. 10c). Interestingly, these models predicted that E6.5 PGC-derived clones stably persist, showing only very little difference in their number and size distribution (Extended Data Fig. 10d,e). We reason that the surviving PGC clones had enlarged enough to be refractory to extinction due to the population effect before compartmentalisation. In contrast, E11.5-gonocyte-derived sub-clones showed high stability in 1D and q-1D models because these clones originated within these geometric restrictions (Extended Data Fig. 10f). Consistently, the local mosaic patch structure was strongly preserved in 1D and q-1D, but not in the global competition model (Fig. 5d and Extended Data Fig. 10g–i). Moreover, the model is consistent with enhanced long-term diversity of previously characterised SSC-derived germ cell clones, which originate after the system reached homeostasis ("sub-sub-clones" in the context of this study) within seminiferous tubules[37,43] (Extended Data Fig. 10j).

347 Importantly, our model also predicts that when an SSC were to emerge with a selective advantage
348 in cell competition (e.g., through a mutation), the expansion of its clone would nevertheless be
349 strongly restricted due to the 1D geometry (Extended Data Fig. 10k).
350 Taken together, these model analyses suggest that the stable persistence of germ cell
351 clones is achieved through the combination of population and geometric effects.
352
353 **Discussion**
354 By integrating *Polylox* barcoding with mathematical modelling, we quantitatively reconstructed
355 the clonal dynamics across the entire lifespan of the mouse male germline. Notably, our analyses
356 revealed that PGC-derived germline clones showed biphasic dynamics: an early phase of clonal
357 "pruning" in which many lineages are lost, followed by a later phase of "preservation", offering
358 an unprecedented bird's-eye view of germline development (Fig. 5e).
359 These clonal dynamics underscore the pivotal role of the germline in preserving
360 genomic integrity across generations. During the early phase, clonal pruning may be critical to
361 establishing the definitive germline, by narrowing the population to cells progressing through
362 sequential developmental processes. The observed stochastic nature of the pruning may, for
363 example, reflect stochastic establishment of germ cell identity followed by survival-based
364 selection of cells best suited for definitive germline, or/and may result from stochastic fluctuations
365 of extracellular environments that instruct germ cell fate deterministically. While the mechanisms
366 that underpin this pruning remain an open question, sparse distribution of PGCs during migration
367 through embryonic tissues[27] may reduce spatial interference and help shape clonal dynamics.
368 Later, once the definitive germline is established, dominance by a limited number of
369 clones may become undesirable, since harmful de novo mutations occurring in SSCs can cause
370 genetic disorders in children. In particular, so-called selfish mutations, which confer a
371 proliferative advantage to SSCs, are known to expand in the testis of ageing men and are
372 associated with severe disorders in offspring[44]. Comparable clonal expansions are also observed
373 in somatic tissues; however, these tissues accumulate mutations at much higher rates than the
374 germline[45,46], and many, including epithelia and blood, develop age-associated patchworks of
375 mutated clones, often marked by well-characterised driver mutations[47]. Most strikingly,
376 haematopoiesis in ageing individuals can become dominated by a small number of driver clones,
377 a universal process known as clonal haematopoiesis[48].
378 These features illustrate the distinct missions of soma and germline, and the distinct
379 demands placed on their respective stem cells. Somatic stem cells must reliably supply

differentiating cells to sustain tissue function and architecture over the individual's lifetime but can tolerate some mutation load, if tissue integrity is preserved. By contrast, SSCs, despite being dispensable for the father's own survival, carry the dual function of sustaining high sperm production and faithful genome transmission for the next generation. Failure to meet either requirement is problematic and results in infertility or the propagation of harmful mutations.

Notably, these germline and somatic stem cell functionality may be linked with the tissue geometry. In epithelia, extended two-dimensional structures permit widespread clonal expansion, while in blood, the mobility of stem cells within the bone marrow facilitates rapid dominance by a few clones, a scenario akin to our global competition model. By contrast, the (quasi-) one-dimensional architecture of seminiferous tubules appears ideally adapted to balance the contradictory demands of high sperm output and control of mutations with selective advantage. As a tubular structure, they possess an extensive surface area able to support high-throughput spermatogenesis, while their one-dimensional organization effectively limits over-representation of particular clones during the prolonged reproductive lifespan.

To conclude, the transition in the germline clonal dynamics from early establishment to sustained homeostasis, reflects a shift in tissue geometry, which is remarkably well-adapted to the germline's unique mission: to maximise reproductive capacity while preserving genomic integrity across generations.

Methods

Mice. *Rosa26*^{Polylox}[12], *CAG-CAT-EGFP*[30], *Dppa3-ECFP*[49], and *Rosa26*^{Confetti}[42] alleles were previously described; *Prdm14-MiCM* allele was newly generated in this study, as detailed in the following section. All these mouse lines were maintained in a C57BL/6J background (purchased from CLEA Japan or Japan SLC). The *Prdm14-MiCM* transgenic mice were generated with approval by Institutional Animal Experiment Committee of the University of Tsukuba. All other animal experiments were approved by Institutional Animal Care and Use Committee of the National Institutes of Natural Sciences.

Generation of a *Prdm14-MiCM* transgenic allele. A bacterial artificial chromosome (BAC) carrying a genome fragment of C57BL/6J mouse spanning the entire *Prdm14* coding sequence plus 157kb flanking sequence (clone RP24-341H14)[22,50] was modified in *E. coli* (Extended Data Fig. 1a). Briefly, exons 2 to 5 of the *Prdm14* gene were replaced by a *Mer-iCre-Mer*[20,21] sequence, polyA signal and the FRT-flanked Neo cassette, using RED recombination system[51] .The loxP and lox511 sites on the vector were replaced with *Amp*^{r} and *Zeo*^{r} genes, respectively. Finally, the Neo cassette was deleted by a transient flippase activation. The resultant, *Prdm14-MiCM* BAC was purified, linearized by PI-SceI digestion, and injected into pronuclei of C57BL/6J mouse zygotes to generate transgenic animals. For G_0 animals, the presence of transgene was examined by PCR using Taq DNA polymerase (BioAcademia) for 5min at 94°C; (20s at 94°C, 20s at 68–61°C, 7s at 72°C) 8 times with 1°C touchdown; (20s at 94°C, 20s at 60°C, 7s at 72°C) 27 times; 14s at 72°C, with primers *MiCM_3UTR_5For* (5'- GCTTATCGACTAATCAGCCATAC -3') and *Prdm14_3arm_MidRev* (5'-CCACCTCACTAAGTTGCTGC-3'), amplifying 336bp sequence of the transgene. For F1 and F2 generations, the transgene copy number was quantified by qPCR using THUNDERBIRD SYBR qPCR Mix (Toyobo) and LightCycler 96 (Roche), for 95°C at 60s; (15s at 95°C, 60s at 40°C) 45 times, with primers *Prdm14_qPCR_5For* (5'-CGTTTCGCTAAACTCCTTGG -3') and *Prdm14_qPCR_5Rev* (5'-TGCAGCCGAGATAGGAGAAG -3') annealing Intron 1 of *Prdm14*, and *b-actin For* (5'-ACCACAGGCATTGTGATGG -3') and *b-actin_Rev* (5'- TCGGTCAGGATCTTCATGAGG -3') as a reference. A transgenic allele with the highest copy numbers at a single locus (line #14) was selected and maintained homozygously (Extended Data Fig. 1b).

4-hydroxytamoxifen administration to pregnant mothers. A stock solution of 4-hydroxytamoxifen (4-OHT; Sigma-Aldrich) was prepared by dissolving 25mg 4-OHT, as well as

432 12.5mg progesterone (Sigma-Aldrich) to sustain pregnancy, into 250µl EtOH and then 2250µl
433 peanut oil (Sigma-Aldrich), using a sonication water bath, and stored at -30°C until use. Male and
434 female mice homozygously carrying the *Prdm14-MiCM* and the *Polylox* alleles, respectively,
435 were crossed to avoid leaky recombination in zygotes due to maternally-derived MiCM protein
436 accumulated in oocytes during oogenesis. After overnight pair housing, a vaginal plug was
437 checked the following morning, with midday on the day of plug detection designated as E0.5. To
438 induce at E6.5&6.75, two successive doses of 150 µl stock solution (containing 1.5 mg 4-OHT)
439 were orally administered at a 6h interval. For E11.5 induction, a dose of 100µl of stock solution
440 (containing 1mg 4-OHT) was administered orally. For a postnatal sampling of the testes, a
441 Caesarean section was performed at E19.5, and the pups were bred by foster mothers (ICR).
442
443 **PGC count.** To count the number of PGCs (or gonocytes/prospermatogonia) with and without
444 barcoding, homozygous *Polylox* females were crossed with males carrying *Prdm14-MiCM* and
445 *Dppa3-ECFP* alleles, generating embryos heterozygous for *Polylox*, *Prdm14-MiCM,* and *Dppa3-*
446 *ECFP*. Testes of these embryos, with 4-OHT administration at E6.5&E6.75 or E11.5, or without
447 administration were harvested at E12.5 and fixed in 4% PFA in PBS for 2h at 4°C. Testes without
448 4-OHT administration were also sampled at E13.5. The samples were washed with PBS
449 containing 0.1% TritonX-100 (PBST), blocked with 4% Donkey serum in PBST at room
450 temperature (RT) for 3h, incubated with primary antibody solution [rabbit anti-DDX4 (Abcam
451 Cat#ab13840, 0.05%) supplemented with 4% donkey serum in PBST] at 4°C overnight, washed
452 with PBST at RT for >1h four times, and incubated in 2nd antibody solution [donkey anti-Rabbit
453 IgG (H+L) Cy3 (Jackson ImmunoResearch 711-165-152, 0.1%) and goat anti-GFP (SICGEN
454 AB0020-200) conjugated with DyLight™ 488 NHS Ester (Thermo Fisher Scientific, 0.1%),
455 supplemented with 4% donkey serum in PBST] at 4°C overnight. After washing with 1mL PBST
456 at RT for >1h four times, the testes were mounted with Scale SQ[52], and serial images were
457 acquired for 3D reconstruction using TCS-SP8 (Leica). To count the number of PGCs
458 automatically, captured images were analysed by custom program written for R software
459 environment (www.r-project.org) with EBImage packages[53]. In brief, PGC masks were created
460 using ECFP and immunostained DDX4 signals by applying Gaussian blur filter followed by local
461 thresholding and size selection. Information of each single PGC across several slices was
462 integrated. PGCs in individual testis cords, obtained from two independent E13.5 testis images,
463 were also counted (Extended Data Fig.8d, upper right).
464

465 **General procedure for barcode sequencing, decoding, and filtering.** The *Polylox* locus was
466 PCR-amplified from genomic DNA samples using primers #2,427 and #2,450[12,54] and KOD FX
467 Neo polymerase (Toyobo) with a thermal cycler MiniAmp Plus (Thermo Fisher Scientific) under
468 a thermal cycling condition of initial denaturation (94°C for 2 min) followed by 28 or 30 cycles
469 of 98°C for 10 sec, 64°C for 30 sec, and 68°C for 150 sec, and a final extension (68°C for 7 min).
470 The amplicons were purified using AMPure XP (Beckman Coulter) at a 1:1 ratio, and proceeded
471 for library preparation using a SMRTbell® Express Template Prep Kit 2.0 (Pacific Biosciences)
472 according to the manufacturer's protocol (101-791-700), and long-read Single Molecule, Real-
473 Time (SMRT) sequencing using Sequel I and Sequel IIe sequencers (Pacific Biosciences) with
474 standard parameters.
475 The obtained circular consensus sequencing (CCS) reads were converted to barcodes,
476 followed by classifying into 'legitimate' barcodes (those which are theoretically possible to occur
477 from the original *Polylox* sequence) and 'illegitimate' barcodes (those which are expected not to
478 occur), as described previously[12,54]. Given the rarity of illegitimate barcode detection and their
479 distinct read number distribution from the vast majority of legitimate barcodes, we reason that
480 these anomalous barcodes likely arose from PCR or bioinformatics processing errors, rather than
481 from genuine recombination events involving the *Polylox* locus within germ cell genomes. This
482 suggests that legitimate barcodes may include some artefacts, so we filtered out rarely observed
483 barcodes altogether so that the illegitimate barcode reads became less than 5% of total reads
484 (Extended Data Fig. 2a).
485
486 **Specificity verification of barcode introduction into PGCs.** Triple transgenic embryos carrying
487 *Polylox*, *Prdm14-MiCM* and *Dppa3-ECFP* alleles resulting from the crossing described
488 previously were barcoded by 4-OHT administration at E6.5&6.75 or E11.5. For each schedule,
489 gonads collected from eight embryos at E12.5 were pooled and dissociated by a Liberase solution
490 [0.5 mg/mL DNase (Worthington), 0.26 U/mL Liberase™ TM (Roche), and 18U /mL Britase
491 (Wako) in PBS]. PGCs and gonadal somatic cells were separately collected as $ECFP^+$ and $ECFP^-$
492 fractions, respectively, using a MA900 cell sorter (Sony) (Supplementary Fig. 1a), and proceeded
493 for genome PCR amplification (30 cycles) and barcode analysis as described above. We found
494 that recombined barcodes were detected only in the $ECFP^+$ fraction sorted from the testes of
495 embryos obtained from 4-OHT injected mothers, with no recombination detected at all in the
496 $ECFP^-$ fraction or samples without 4-OHT injection, verifying that barcode recombination
497 occurred in a high germ cell-specific and tamoxifen-dependent manner (Extended Data Fig. 1e).

498

499 **Barcode analysis of developing and adult germ cells.** To observe the clonal dynamics during
500 development, embryos carrying *Polylox* and *Prdm14-MiCM* alleles were barcoded at E6.5&6.75
501 or E11.5, followed by harvesting posterior-half embryos at E8.5 (for E6.5&6.75-labeled embryos
502 only) or bilateral testes at time points spanning from E12.5 to 1Y. Samples harvested at embryonic
503 stages, i.e., posterior-half embryos and testes after removing the mesonephros, were lysed
504 separately in 16μl protease solution; all the template DNA was directly used for PCR
505 amplification (28 cycles) and barcode analyses. Postnatally, right and left testes were
506 independently collected, removed off the tunica albuginea, lysed in 200–1000μl protease solution
507 followed by DNA purification, and 100–1000 ng template DNA (representing 1.7×10^4–10^5 cells)
508 was used for barcode PCR amplification (28–30 cycles) and barcode analysis. To calculate the
509 barcode compositions per individual, barcode reads from bilateral testes were combined based on
510 the assumption that the germ cell numbers were equal between testes.

511 We found that ~4% of these double-transgenic mice harboured recombined barcode
512 sequences broadly over somatic cells, likely due to leaky and 4-OHT-independent recombination
513 during very early development. Accordingly, barcode sequencing was performed on samples
514 taken from individuals whose somatic tissues (head or tail, respectively, for samples taken at E8.5
515 or other stages) were confirmed by PCR amplification to have full-length *Polylox* sequences only.
516 Further, the sex of the E8.5 and E12.5 embryos were determined by PCR amplification of the
517 *Rbm31x/y* genes[55].

518 Barcode sequencing of individual E13.5 PGCs (Extended Data Fig. 2d), isolated by
519 FACS-sorting of the Dppa3-ECFP+ population (Supplementary Fig. 1a), was performed similarly
520 to that of undifferentiated spermatogonia, as described below.

521

522 **Verification that the barcode reads linearly reflect the cell composition.** Considering the
523 possibility of biased PCR-amplification, library construction and sequencing, we verified if and
524 how much the composition of the barcode reads mirrors that of cells carrying heterogeneous
525 barcodes. Testes from adult mice barcoded at E6.5&6.75 were dissociated by a Liberase solution
526 (see above), and were incubated in antibody solution [Alexa Fluor 647-conjugated rat anti-CD9
527 (BioLegend 124810, 1:500, PECy7-conjugated rat anti-KIT (BioLegend 105814, 1:200) and
528 Brilliant Violet 421-conjugated rat anti-CD324 (BioLegend 147319, 1:1000) in PBS] on ice for
529 30 min. Then, a $CDH1^+/CD9^+/KIT^-$ undifferentiated spermatogonia fraction was collected by an
530 MA900 cell sorter (Sony), as a bulk of 17,000 to 25,000 cells and in parallel as a separate

531 assembly of hundreds of individual cells (Supplementary Fig. 1b). Barcode analyses through
532 PCR-amplification and amplicon long-read sequencing were conducted as described previously.
533 In parallel, barcodes are also decoded separately in individual cells by Sanger sequencing
534 (Fasmac) of the *Polylox* sequence amplified by nested PCR. The primers used are #2,450 and
535 #494 for the first round, and #2,426 and #2,427 for the second round, respectively[12]. Both rounds
536 of PCR were performed using KOD FX Neo at 25μl scale and the following protocol: 2 min at
537 94°C followed by 25 rounds of (10s at 98°C, 30s at 64°C, 2min30sec at 68°C) and 7min at 68°C.
538 1μl of the 1st PCR product was used as a template for the 2nd PCR. The products of the second
539 PCR were treated with ExoSAP-IT Express (Thermo Fisher Scientific) and were sequenced with
540 primers #2,427, #2,450, #2,623 (5′-AGAAGTTGCATACACAGTATTG-3′) or #2,622 (′-
541 ATCATCGAGCTCGTCAACAATG-3′)[12]. A custom script (SangerSeqSingleFilesAnalysis.m
542 from Daniel Postrach) was used to determine barcode elements in sequencing reads.
543 We found a strong linear correlation between the frequency of barcode reads obtained
544 from the bulk population using deep sequencing and the number of cells whose barcode was
545 individually determined (Extended Data Fig. 2c). We concluded that the barcode frequencies
546 obtained from bulk Sequel deep sequencing faithfully reflect the composition of cell numbers
547 with these barcodes within the population of interest and that the technical biases, if any, are
548 negligible.
549
550 **Comparison of barcode distributions between the SSC pool, spermatogenesis, and offspring.**
551 Four male mice barcoded at E6.5&6.75 were each crossed with multiple ICR females from 8–9
552 weeks old. Because the males heterozygously harboured the *Polylox* transgene, about half of the
553 offspring inherited barcodes via sperm. The fathers were sacrificed at 1 year of age, whose right
554 and left testes were separately dissociated using a Liberase solution (see above). Half of the
555 dissociated cells were used to FACS-sort a "SSCs" (i.e., $CDH1^{+}CD9^{+}KIT^{-}$ undifferentiated
556 spermatogonia) fraction (Supplementary Fig. 1b), while the other half were directly proceeded as
557 "spermatogenesis" fraction without sorting, for amplicon sequencing as described previously to
558 gain barcode reads. In parallel, the offspring's tail tips were digested by Cica Genius AN (Kanto
559 Chemical) to prepare the DNA, followed by PCR-amplification of the *Polylox* sequence using
560 KOD FX Neo with the temperature condition of 2 min at 94°C followed by 32 rounds of (10s at
561 98°C, 30s at 64°C, 2min30sec at 68°C) and 7min at 68°C, using primers #2,427 and #2,450. PCR
562 products were treated with ExoSAP-IT Express, and barcodes were sequenced in the same way
563 as single-cell-derived barcodes (see above). Temporal bias of barcode appearance in offspring

564 was evaluated using the methods detailed in the Supplementary Methods.
565
566 **Visualization of *Prdm14*$^{+}$ cell clones using a fluorescence reporter.** To visualize the spatial
567 distribution of the descendants of cells expressing *Prdm14* at E6.5&6.75, homozygous *CAG-CAT-*
568 *EGFP* females were crossed with homozygous *Prdm14-MiCM* males to conceive embryos
569 carrying *Prdm14-MiCM* and *CAG-CAT-EGFP* alleles heterozygously. Following 4-OHT
570 administration to pregnant mothers at E6.5&6.75, whole embryos and posterior-half embryos
571 were harvested at E7.5 and E8.5, respectively, and fixed in 4% PFA in PBS for 2h at 4°C. After
572 washing with PBST, the samples were blocked with 4% Donkey serum in PBST containing 0.1%
573 Hoechst 33342 (Thermo Fisher Scientific) and incubated for 3h at RT. Then, the blocking solution
574 was switched to the primary antibody solution [anti-GFP (goat, Sicgen AB0020-200; rat, Nacalai
575 Tesque 04404-84; or chicken, Aves Labs GFP-1010), together with rabbit anti-OCT4 (Abcam
576 ab181557), and with or without goat anti-FoxF1 (R&D Systems AF4798); all used at 0.1%, and
577 supplemented with 4% donkey serum in PBST], and the samples were incubated at 4°C overnight
578 (>16h). Afterwards, samples were washed with PBST at RT for >1h four times, and incubated in
579 the secondary antibody solution [any one of anti-Goat IgG (H+L) Alexa 488 (705-545-147), anti-
580 Rat IgG (H+L) Alexa 488 (712-545-153) or anti-Chicken IgY (H+L) Alexa 488 (703-545-155),
581 together with anti-Rabbit IgG (H+L) Cy3 (711-165-152), and with or without anti-Goat IgG
582 (H+L) Alexa 647 (705-605-147); all donkey-derived (Jackson ImmunoResearch), used in 0.1%,
583 and supplemented with 4% donkey serum in PBST] at 4°C overnight. After washing with PBST
584 at RT for >1h four times, the samples were mounted using Scale SQ[52], and serial images were
585 acquired for 3D reconstruction with a TCS-SP8 confocal microscope (Leica). Three-dimensional
586 visualisation was performed using ClearVolume[56].
587
588 **Barcode analysis of seminiferous tubule fragments.** To address the spatial distribution of
589 barcoded clones over seminiferous tubules, the testes of two E6.5&6.75-barcoded male mice were
590 obtained at 8–9 weeks of age. For each mouse, one of the testes was lysed for barcode amplicon
591 sequencing as described earlier to verify the degree of recombination; the other was extensively
592 disentangled to collect virtually the entire seminiferous tubule length in as long fragments as
593 possible. Fragments 4cm or longer were cut into sub-fragments. Genomic DNA purified from
594 each of these (sub)fragments was used for amplicon-sequencing to determine the barcode
595 composition included therein. For each fragment, barcodes with <1% read frequency were filtered
596 out because they were likely due to contaminated germ cells from other fragments during

sampling. To estimate the length of tubule segments occupied by cells with each barcode, its read frequency was multiplied by the length of the fragments from which the barcode was yielded. The number of SSCs in each fragment was estimated by multiplying its length by 30 cells per millimeter[57].

Multi-colour reporter observation of PGC clones in seminiferous tubules. Homozygous *Rosa26*^{Confetti} females were crossed with homozygous *Prdm14-MiCM* males to obtain foetus that obtain both genes heterozygously. After 4-OHT administration at E6.5&6.75 and Caesarean section as in the same way with barcoding procedure, seminiferous tubules of bilateral testes obtained from males between 29 and 36 days old were untangled thoroughly and fixed in 4% PFA in PBS for 1h at 4°C. Followed by washing with PBST, the fluorescent images of seminiferous tubules were obtained using a M165FC stereoscopic microscope (Leica) with GFP-LP, RFP-LP and ET-CFP filters. Green signals were regarded as cYFP but not nGFP according to their localisation in the cytoplasm. We could not find an ECFP signal, possibly because the mECFP cassette was not activated by recombination or the mECFP signal was not strong enough to be distinguished from background signals. Because we found clear cYFP and cRFP signals in only limited areas in 5 out of 9 mice (Extended Data Fig. 9a), we reasoned that recombination occurred infrequently, and labelled cells derived from only one or a few PGCs at E6.5&E6.75.

Mathematical modelling of clonal PGC dynamics. Methods and theory for the modelling of clonal PGC dynamics are detailed in Supplementary Methods and Supplementary Equations. In brief, we modelled cellular dynamics of division, migration, loss and spatial organisation following clones of the emerging E6.5 PGCs. The cellular dynamics of PGC clones were simulated alongside *Polylox* barcode recombination, to infer key biological insights from multiple aspects of the experimental barcoding data. Namely, the reduction of clonal diversity in the embryo, followed by the maintenance of the survivors, and the spatial organisation of these clones in the testes over the murine life span. We investigated mechanism for the postnatal stability of PGC clones, incorporating the specific geometry of the seminiferous tubules in the testes shaping competition of the SSC clones emerging from the PGCs.

Code availability. All code for mathematical modelling was written in the Julia programming language and is available on GitHub. The complete executing code for clonal PGC dynamics is contained in GermlineDynamics (https://github.com/hoefer-lab/GermlineDynamics). Code

therein calls methods for *Polylox* barcode simulation and inference from the package PolyloxMechanics.jl (https://github.com/hoefer-lab/PolyloxMechanics.jl). All Bayesian inferences are based on methods from the package ABCdeZ.jl (https://github.com/hoefer-lab/ABCdeZ.jl). During the review process 'GermlineDynamics' and 'PolyloxMechanics.jl' (as of now private repositories) are available at ***** (Password: *****). The custom programs used for counting the number of PGCs, and all the other calculations for plotting written as R markdown documents, are available upon request.

Data availability. All barcode CCS data are archived in DDBJ Sequence Read Archive (DRA) and will be available upon peer-reviewed publication. All Sanger sequence reads will also be available upon request after peer-reviewed publication. The image datasets will be available at SSBD:repository upon peer-reviewed publication.

Acknowledgements

We thank the members of the NIBB Yoshida lab, the DKFZ Höfer lab, A. Goriely (Oxford University), and N. Honda (Nagoya University) for discussion, NIBB Model Organisms Facility for animal care, NIBB Trans-Omics Facility for Sequel sequencing, T. Feyerabend for a *Rosa26*^{Polylox} mouse strain, M. Saitou, K. Hayashi and G. Nagamatsu for a *Dppa3-ECFP* mouse strain, M. Saitou, H. Ohta and K. Kurimoto for a BAC clone, K. Busch and M. Reth for a *Mer-iCre-Mer* construct, and X. Wang, J. Rößler and D. Postrach for scripts to determine *Polylox* barcodes. This work is funded by MEXT and JSPS (Grant-in-Aid for Scientific Research KAKENHI JP25114004, JP15K21736, JP17K19413, JP18H05551, and JP23H04952 to S.Y.; and JP17H07335, JP19J00410, JP21K15111, JP22H05639, JP24H01413, and JP24K18129 to T.I.), and AMED (AMED-ASPIRE, 25jf0126012h0001 and 26jf0126012h0002 to S.Y.). TI was supported by the JSPS Research Fellowship for Young Scientists (JP19J00410). M.L. was supported by the Helmholtz Graduate School for Cancer Research fellowship. T.H. was supported by Sonderforschungsbereich (SFB 873-B11) and DKFZ core funding.

Author contributions

T.I. performed most of the experiments, with the support of C.K. and A.M.; T.I., M.L., and T.Ni. performed barcode calculations and statistical evaluations; M.L. designed and performed mathematical modelling of clonal/barcode dynamics, with input from T.Ni. and T.H.; Y.K.

developed an algorithm to count PGCs; K.Ya. and S.Sh. performed SMRT sequencing and initial data mining; M.L. and K.Yo. performed time-series mathematical analysis of barcode appearance in offspring; T.I., S.Su. and T.Na. conducted cell sorting; S.M. and S.T. established a *Prdm14-MiCM* by microinjection; T.I. and S.Y. designed the experiments; T.I., M.L., T.H., and S.Y. wrote the manuscript with input from all contributors; S.Y., H.-R.R., and T.H. conceived and supervised the study.

Author information

These authors contributed equally: Tatsuro Ikeda, Maurice Langhinrichs

Competing interests

These authors declare no competing interests.

Additional information

Supplementary Information is available for this paper.

Supplementary Fig. 1. Gating strategy for embryonic PGCs and gonadal somatic cells (a), and adult SSCs (b).

Supplementary Table 1. List of mice subjected to barcode bulk sequencing in this study.

Supplementary Table 2. Number of testicular PGCs quantified by image analysis.

Supplementary Table 3. Barcodes detected in E8.5 embryos and in FACS-sorted adult bulk SSCs after E6.5-barcoding.

Supplementary Table 4. Barcodes detected in bilateral testes after E6.5-barcoding.

Supplementary Table 5. Barcodes detected in individual E13.5 PGCs or adult SSCs.

Supplementary Table 6. Barcodes detected in individual offspring of E6.5-barcoded males.

Supplementary Table 7. Number of GFP+ cells in E7.5 and E8.5 embryos.

Supplementary Table 8. Barcodes detected in bilateral testes after E11.5-barcoding.

Supplementary Table 9. List of seminiferous tubule fragments analysed in E6.5-barcoded mice.

Supplementary Table 10. Barcodes detected in seminiferous tubule fragments

Supplementary Table 11. Number of PGCs in E13.5 testis cords quantified by image analysis.

Supplementary Methods

Supplementary Equations

Correspondence and requests for materials should be addressed to Thomas Höfer and Shosei Yoshida.

696 ## References

697 1 Molyneaux, K. & Wylie, C. Primordial germ cell migration. *Int J Dev Biol* **48**, 537-544
698 (2004). https://doi.org/10.1387/ijdb.041833km
699 2 Saitou, M. & Yamaji, M. Primordial Germ Cells in Mice. *Csh Perspect Biol* **4** (2012).
700 https://doi.org/10.1101/cshperspect.a008375
701 3 Combes, A. N. *et al.* Three-dimensional visualization of testis cord morphogenesis, a
702 novel tubulogenic mechanism in development. *Dev Dyn* **238**, 1033-1041 (2009).
703 https://doi.org/10.1002/dvdy.21925
704 4 Western, P. S., Miles, D. C., van den Bergen, J. A., Burton, M. & Sinclair, A. H. Dynamic
705 regulation of mitotic arrest in fetal male germ cells. *Stem Cells* **26**, 339-347 (2008).
706 https://doi.org/10.1634/stemcells.2007-0622
707 5 Nagano, R. *et al.* Reproliferation and relocation of mouse male germ cells (gonocytes)
708 during prespermatogenesis. *Anat Rec* **258**, 210-220 (2000).
709 https://doi.org/10.1002/(SICI)1097-0185(20000201)258:2<210::AID-AR10>3.0.CO;2-
710 X
711 6 Yoshida, S. Heterogeneous, dynamic, and stochastic nature of mammalian spermatogenic
712 stem cells. *Curr Top Dev Biol* **135**, 245-285 (2019).
713 https://doi.org/10.1016/bs.ctdb.2019.04.008
714 7 Lawson, K. A. & Hage, W. J. Clonal Analysis of the Origin of Primordial Germ-Cells in
715 the Mouse. *Ciba F Symp* **182**, 68-84 (1994). https://doi.org/10.1002/9780470514573.ch5
716 8 Ueno, H., Turnbull, B. B. & Weissman, I. L. Two-step oligoclonal development of male
717 germ cells. *Proc Natl Acad Sci U S A* **106**, 175-180 (2009).
718 https://doi.org/10.1073/pnas.0810325105
719 9 Nguyen, D. H. *et al.* Apoptosis in the fetal testis eliminates developmentally defective
720 germ cell clones. *Nat Cell Biol* **22**, 1423-+ (2020). https://doi.org/10.1038/s41556-020-
721 00603-8
722 10 Lei, L. & Spradling, A. C. Mouse primordial germ cells produce cysts that partially
723 fragment prior to meiosis. *Development* **140**, 2075-2081 (2013).
724 https://doi.org/10.1242/dev.093864
725 11 McKenna, A. *et al.* Whole-organism lineage tracing by combinatorial and cumulative
726 genome editing. *Science* **353**, aaf7907 (2016). https://doi.org/10.1126/science.aaf7907
727 12 Pei, W. *et al.* Polylox barcoding reveals haematopoietic stem cell fates realized in vivo.
728 *Nature* **548**, 456-460 (2017). https://doi.org/10.1038/nature23653

13 Pei, W. *et al.* Resolving Fates and Single-Cell Transcriptomes of Hematopoietic Stem Cell Clones by PolyloxExpress Barcoding. *Cell Stem Cell* **27**, 383-395 e388 (2020). https://doi.org/10.1016/j.stem.2020.07.018

14 Kalhor, R. *et al.* Developmental barcoding of whole mouse via homing CRISPR. *Science* **361** (2018). https://doi.org/10.1126/science.aat9804

15 Alemany, A., Florescu, M., Baron, C. S., Peterson-Maduro, J. & van Oudenaarden, A. Whole-organism clone tracing using single-cell sequencing. *Nature* **556**, 108-112 (2018). https://doi.org/10.1038/nature25969

16 Spanjaard, B. *et al.* Simultaneous lineage tracing and cell-type identification using CRISPR-Cas9-induced genetic scars. *Nat Biotechnol* **36**, 469-473 (2018). https://doi.org/10.1038/nbt.4124

17 Bowling, S. *et al.* An Engineered CRISPR-Cas9 Mouse Line for Simultaneous Readout of Lineage Histories and Gene Expression Profiles in Single Cells. *Cell* **181**, 1693-1694 (2020). https://doi.org/10.1016/j.cell.2020.06.018

18 Weber, T. S. *et al.* LoxCode in vivo barcoding reveals epiblast clonal fate bias to fetal organs. *Cell* **188**, 3882-3896 e3819 (2025). https://doi.org/10.1016/j.cell.2025.04.026

19 Chan, M. M. *et al.* Molecular recording of mammalian embryogenesis. *Nature* **570**, 77-82 (2019). https://doi.org/10.1038/s41586-019-1184-5

20 Busch, K. *et al.* Fundamental properties of unperturbed haematopoiesis from stem cells in vivo. *Nature* **518**, 542-546 (2015). https://doi.org/10.1038/nature14242

21 Zhang, Y. *et al.* Inducible site-directed recombination in mouse embryonic stem cells. *Nucleic Acids Res* **24**, 543-548 (1996). https://doi.org/10.1093/nar/24.4.543

22 Yamaji, M. *et al.* Critical function of Prdm14 for the establishment of the germ cell lineage in mice. *Nat Genet* **40**, 1016-1022 (2008). https://doi.org/10.1038/ng.186

23 Seki, Y. *et al.* Cellular dynamics associated with the genome-wide epigenetic reprogramming in migrating primordial germ cells in mice. *Development* **134**, 2627-2638 (2007). https://doi.org/10.1242/dev.005611

24 Tam, P. P. L. & Snow, M. H. L. Proliferation and Migration of Primordial Germ-Cells during Compensatory Growth in Mouse Embryos. *J Embryol Exp Morph* **64**, 133-147 (1981). https://doi.org/10.1242/dev.64.1.133

25 Mikedis, M. M. & Downs, K. M. STELLA-positive subregions of the primitive streak contribute to posterior tissues of the mouse gastrula. *Dev Biol* **363**, 201-218 (2012). https://doi.org/10.1016/j.ydbio.2011.10.003

26 Mikedis, M. M. & Downs, K. M. PRDM1/BLIMP1 is widely distributed to the nascent fetal-placental interface in the mouse gastrula. *Dev Dynam* **246**, 50-71 (2017). https://doi.org/10.1002/dvdy.24461

27 McDole, K. *et al.* In Toto Imaging and Reconstruction of Post-Implantation Mouse Development at the Single-Cell Level. *Cell* **175**, 859-876 e833 (2018). https://doi.org/10.1016/j.cell.2018.09.031

28 Runyan, C. *et al.* Steel factor controls midline cell death of primordial germ cells and is essential for their normal proliferation and migration. *Development* **133**, 4861-4869 (2006). https://doi.org/10.1242/dev.02688

29 Stallock, J., Molyneaux, K., Schaible, K., Knudson, C. M. & Wylie, C. The pro-apoptotic gene Bax is required for the death of ectopic primordial germ cells during their migration in the mouse embryo. *Development* **130**, 6589-6597 (2003). https://doi.org/10.1242/dev.00898

30 Kawamoto, S. *et al.* A novel reporter mouse strain that expresses enhanced green fluorescent protein upon Cre-mediated recombination. *Febs Lett* **470**, 263-268 (2000). https://doi.org/10.1016/s0014-5793(00)01338-7

31 Mahlapuu, M., Ormestad, M., Enerback, S. & Carlsson, P. The forkhead transcription factor Foxf1 is required for differentiation of extra-embryonic and lateral plate mesoderm. *Development* **128**, 155-166 (2001). https://doi.org/10.1242/dev.128.2.155

32 Gill, M. E., Hu, Y. C., Lin, Y. & Page, D. C. Licensing of gametogenesis, dependent on RNA binding protein DAZL, as a gateway to sexual differentiation of fetal germ cells. *Proc Natl Acad Sci U S A* **108**, 7443-7448 (2011). https://doi.org/10.1073/pnas.1104501108

33 Hu, Y. C. *et al.* Licensing of primordial germ cells for gametogenesis depends on genital ridge signaling. *PLoS Genet* **11**, e1005019 (2015). https://doi.org/10.1371/journal.pgen.1005019

34 Nicholls, P. K. *et al.* Mammalian germ cells are determined after PGC colonization of the nascent gonad. *Proc Natl Acad Sci U S A* **116**, 25677-25687 (2019). https://doi.org/10.1073/pnas.1910733116

35 Hadas, R. *et al.* Temporal BMP4 effects on mouse embryonic and extraembryonic development. *Nature* **634**, 652-661 (2024). https://doi.org/10.1038/s41586-024-07937-5

36 Nakagawa, T., Nabeshima, Y. & Yoshida, S. Functional identification of the actual and potential stem cell compartments in mouse spermatogenesis. *Dev Cell* **12**, 195-206 (2007).

https://doi.org/10.1016/j.devcel.2007.01.002

37 Klein, A. M., Nakagawa, T., Ichikawa, R., Yoshida, S. & Simons, B. D. Mouse germ line stem cells undergo rapid and stochastic turnover. *Cell Stem Cell* **7**, 214-224 (2010). https://doi.org/10.1016/j.stem.2010.05.017

38 Nakata, H. *et al.* Three-dimensional structure of seminiferous tubules in the adult mouse. *J Anat* **227**, 686-694 (2015). https://doi.org/10.1111/joa.12375

39 Clermont, Y. H., C. Microscopic anatomy of the sex cords and seminiferous tubules in growing and adult male albino rats. *American Journal of Anatomy* **108**, 79–97 (1961). https://doi.org/10.1002/aja.1001080106

40 Vergouwen, R. P. *et al.* Postnatal development of testicular cell populations in mice. *J Reprod Fertil* **99**, 479-485 (1993). https://doi.org/10.1530/jrf.0.0990479

41 Vergouwen, R. P. F. A., Jacobs, S. G. P. M., Huiskamp, R., Davids, J. A. G. & Derooij, D. G. Proliferative Activity of Gonocytes, Sertoli Cells and Interstitial-Cells during Testicular Development in Mice. *J Reprod Fertil* **93**, 233-243 (1991). https://doi.org/10.1530/jrf.0.0930233

42 Snippert, H. J. *et al.* Intestinal crypt homeostasis results from neutral competition between symmetrically dividing Lgr5 stem cells. *Cell* **143**, 134-144 (2010). https://doi.org/10.1016/j.cell.2010.09.016

43 Hara, K. *et al.* Mouse spermatogenic stem cells continually interconvert between equipotent singly isolated and syncytial states. *Cell Stem Cell* **14**, 658-672 (2014). https://doi.org/10.1016/j.stem.2014.01.019

44 Goriely, A. & Wilkie, A. O. Paternal age effect mutations and selfish spermatogonial selection: causes and consequences for human disease. *Am J Hum Genet* **90**, 175-200 (2012). https://doi.org/10.1016/j.ajhg.2011.12.017

45 Uchimura, A. *et al.* Early embryonic mutations reveal dynamics of somatic and germ cell lineages in mice. *Genome Res* **32**, 945-955 (2022). https://doi.org/10.1101/gr.276363.121

46 Milholland, B. *et al.* Differences between germline and somatic mutation rates in humans and mice. *Nat Commun* **8**, 15183 (2017). https://doi.org/10.1038/ncomms15183

47 Martincorena, I. Somatic mutation and clonal expansions in human tissues. *Genome Med* **11**, 35 (2019). https://doi.org/10.1186/s13073-019-0648-4

48 Jaiswal, S. & Ebert, B. L. Clonal hematopoiesis in human aging and disease. *Science* **366** (2019). https://doi.org/10.1126/science.aan4673

49 Ohinata, Y., Sano, M., Shigeta, M., Yamanaka, K. & Saitou, M. A comprehensive, non-

828 invasive visualization of primordial germ cell development in mice by the Prdm1-
829 mVenus and Dppa3-ECFP double transgenic reporter. *Reproduction* **136**, 503-514 (2008).
830 https://doi.org/10.1530/Rep-08-0053
831 50 Yamaji, M. *et al.* PRDM14 ensures naive pluripotency through dual regulation of
832 signaling and epigenetic pathways in mouse embryonic stem cells. *Cell Stem Cell* **12**,
833 368-382 (2013). https://doi.org/10.1016/j.stem.2012.12.012
834 51 Lee, E. C. *et al.* A highly efficient Escherichia coli-based chromosome engineering
835 system adapted for recombinogenic targeting and subcloning of BAC DNA. *Genomics*
836 **73**, 56-65 (2001). https://doi.org/10.1006/geno.2000.6451
837 52 Hama, H. *et al.* Sca/eS: an optical clearing palette for biological imaging. *Nat Neurosci*
838 **18**, 1518-+ (2015). https://doi.org/10.1038/nn.4107
839 53 Pau, G., Fuchs, F., Sklyar, O., Boutros, M. & Huber, W. EBImage--an R package for
840 image processing with applications to cellular phenotypes. *Bioinformatics* **26**, 979-981
841 (2010). https://doi.org/10.1093/bioinformatics/btq046
842 54 Pei, W. *et al.* Using Cre-recombinase-driven Polylox barcoding for in vivo fate mapping
843 in mice. *Nat Protoc* **14**, 1820-1840 (2019). https://doi.org/10.1038/s41596-019-0163-5
844 55 Tunster, S. J. Genetic sex determination of mice by simplex PCR. *Biol Sex Differ* **8** (2017).
845 https://doi.org/10.1186/s13293-017-0154-6
846 56 Royer, L. A. *et al.* ClearVolume: open-source live 3D visualization for light-sheet
847 microscopy. *Nat Methods* **12**, 480-481 (2015). https://doi.org/10.1038/nmeth.3372
848 57 Kitadate, Y. *et al.* Competition for Mitogens Regulates Spermatogenic Stem Cell
849 Homeostasis in an Open Niche. *Cell Stem Cell* **24**, 79-+ (2019).
850 https://doi.org/10.1016/j.stem.2018.11.013
851 58 Yoshida, S. *et al.* The first round of mouse spermatogenesis is a distinctive program that
852 lacks the self-renewing spermatogonia stage. *Development* **133**, 1495-1505 (2006).
853 https://doi.org/10.1242/dev.02316
854 59 Nakagawa, T. *et al.* A multistate stem cell dynamics maintains homeostasis in mouse
855 spermatogenesis. *Cell Rep* **37**, 109875 (2021).
856 https://doi.org/10.1016/j.celrep.2021.109875
857 60 Kanatsu-Shinohara, M., Naoki, H. & Shinohara, T. Nonrandom Germline Transmission
858 of Mouse Spermatogonial Stem Cells. *Dev Cell* **38**, 248-261 (2016).
859 https://doi.org/10.1016/j.devcel.2016.07.011
860 61 Bailey, N. T. J. *The elements of stochastic processes with applications to the natural*

sciences. (Wiley, 1964).

62 Klein, A. M. & Simons, B. D. Universal patterns of stem cell fate in cycling adult tissues. *Development* **138**, 3103-3111 (2011). https://doi.org/10.1242/dev.060103

63 Heathcote, C. R. & Moyal, J. E. The Random Walk [in Continuous Time] and Its Application to the Theory of Queues. *Biometrika* **46**, 400-411 (1959). https://doi.org/10.1093/biomet/46.3-4.400

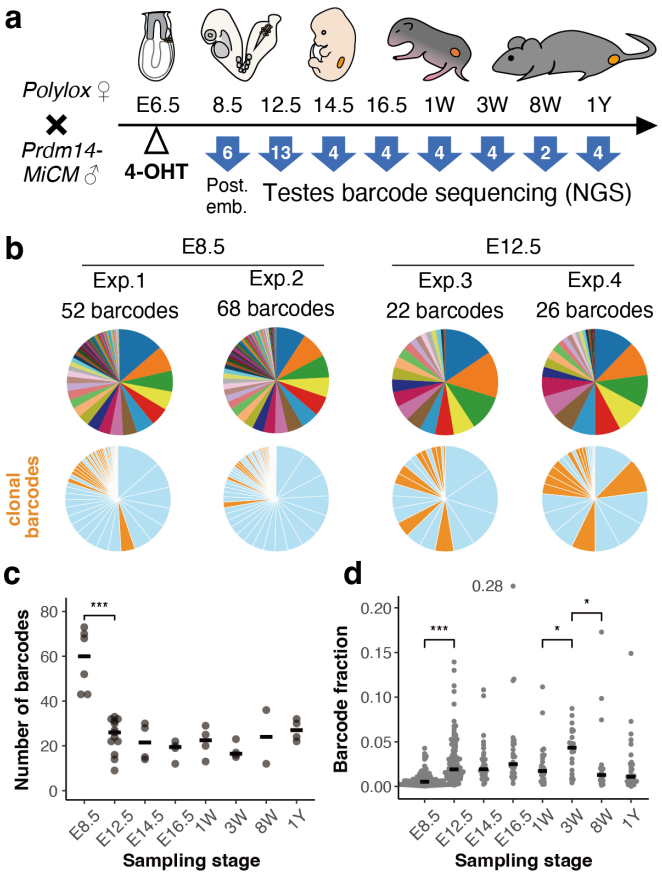

Figure 1. Barcode analysis of E6.5-labeled PGC clones

a, Experimental overview. *Prdm14-MiCM*;*Polylox* male embryos were barcoded at E6.5, whose barcodes in germline were analysed at the indicated time points from individuals of indicated numbers shown in arrows. Week (W); year (Y). The barcode reads obtained from the testes of 1Y-old mice were from experiments detailed in Fig. 2.

b, Representative distribution of barcode reads found in two embryos each at E8.5 and E12.5, displayed in pie charts. Unrecombined barcodes are excluded. Orange highlighted in lower pie charts indicates "clonal barcodes", whose generation probability P_{gen} are low (<0.001), enough to be postulated to be introduced in a single PGC.

c, Barcode diversity found in individual mice (grey dots).

d, The contribution of individual clonal barcodes (P_{gen}<0.001) in all recombined barcodes recovered from each mouse. In (**c**) and (**d**), values only between neighbouring time points were statistically evaluated. Horizontal bars indicate medians. ***p<0.001, *p<0.05, two-sided Mann-Whitney-Wilcoxon test (MWW). The transient increase in clone size variation at 3W might reflect the first round of spermatogenesis, which is still ongoing at this stage[58].

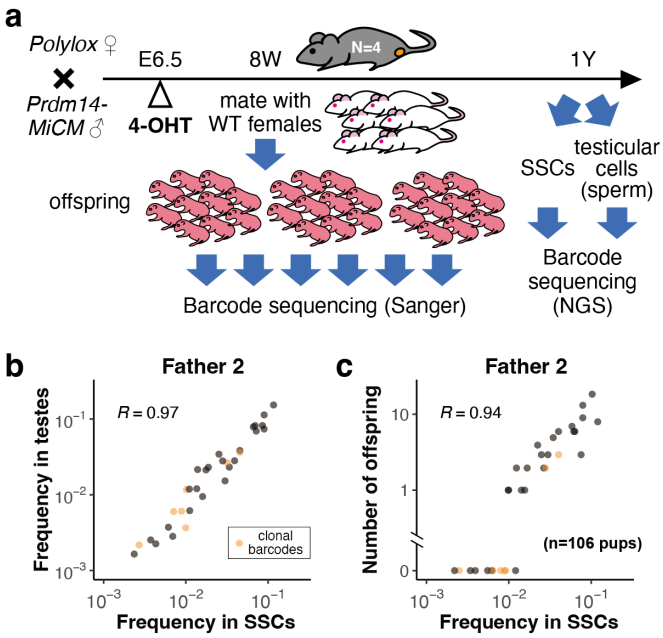

885

886 **Figure 2. Barcode transmission from SSCs through spermatogenesis to offspring**

887 **a**, Experimental overview. Four *Prdm14-MiCM*;*Polylox* male mice barcoded at E6.5 were
888 repeatedly mated with multiple females to give rise to a substantial number of offspring till 1Y
889 old. Barcodes transmitted into offspring were determined individually by Sanger sequencing.
890 Then, the fathers were sacrificed and the barcodes included in their SSCs (specifically,
891 undifferentiated spermatogonia) and bulk testicular cells (representing active spermatogenesis)
892 were analysed by deep-sequencing. Given the heterozygosity of the fathers, approximately half
893 embryos inherit the barcodes.

894 **b**,**c**, Correlation between barcode compositions in SSCs and the bulk testes (**b**), and between
895 father's SSCs and the 106 offspring that harboured barcodes (**c**). Representative data obtained
896 from one male mouse (Father 2) are indicated; see Extended Data Fig. 3 for those from the other
897 fathers. For SSCs and bulk testis, barcodes from each of the bilateral testes were summed with a
898 1:1 ratio. "clonal barcodes" (P_{gen}<0.001) are highlighted in orange. In (**c**), actual number of
899 offspring with barcodes are indicated. Spearman correlation coefficients are indicated.

900

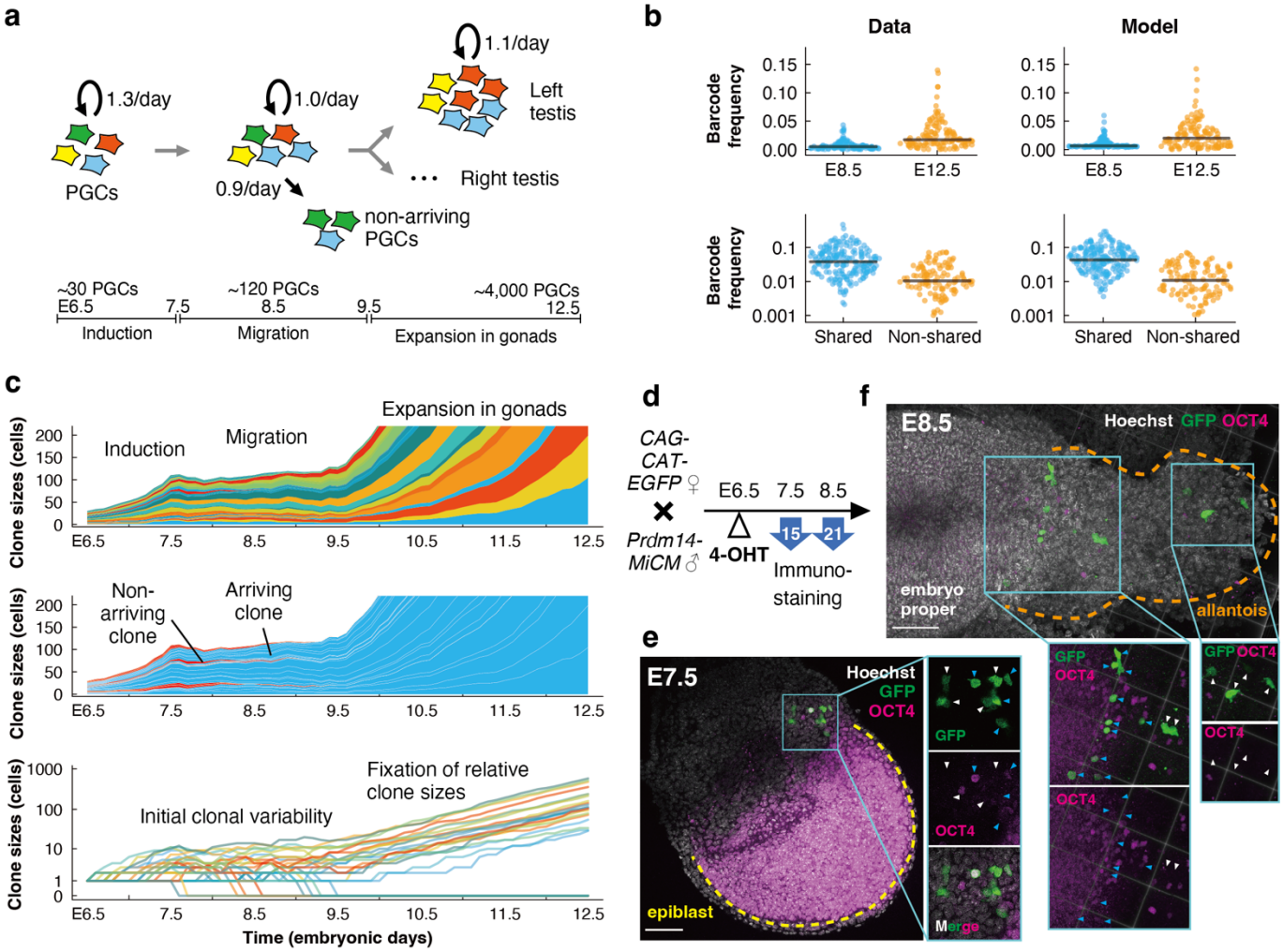

Figure 3. Inference of clonal dynamics of PGCs from E6.5 to E12.5

a, Scheme of the "top model" with parameters inferred from E6.5 PGC-barcoding data. In this scheme, the initial ~30 PGC clones proliferate through sequential phases of neutral birth-death processes, reaching the left and right gonads at expanded clone sizes. During the migration phase (E7.5–9.5) a non-arriving fraction of PGCs emerges that lost the ability to reach the gonads. The class of birth-death processes was informed by rescaled clone size distributions (Extended Data Fig. 4; Supplementary Methods). Different models were tested and fitted on barcode, cell number and sharing statistics, among which this top model was found to be best-fit (Extended Data Fig. 5a).

b, Predictive capacity of the top model (right) for a dataset not used for fitting (left). The frequency of clonal *Polylox* barcodes among all recombined barcodes for both measurement time points (top panels; model shows a representative simulation). Barcode frequencies (all

914 except unrecombined) at E12.5 distinguishing barcodes shared and non-shared between bilateral
915 testes (bottom panels). Horizontal lines indicate medians.
916 **c**, Model prediction of the clonal dynamics of PGCs. Model inference was conducted based on
917 *Polylox* barcodes, followed by re-simulations for individual clones originating from a single cell
918 at E6.5. Clone size dynamics of the re-simulated ~30 PGC clones were shown in different
919 colours (top panel), arriving (blue) and non-arriving (red) clones (middle panel). Clone size
920 evolution plotted on log-scale (bottom panel), indicating that early stochastic fluctuation in
921 clone size become stabilised by ~E11, after which clones expanded proportionally.
922 **d**, Experimental overview for (**e**) and (**f**). Following induction by 4-OHT administration at E6.5,
923 GFP-labelled cells in *Prdm14-MiCM*;*CAG-CAT-EGFP* embryos were analysed at E7.5 and E8.5
924 for their distribution and marker protein expression.
925 **e**,**f**, E7.5 (**e**) and E8.5 (**f**) embryos, immunostained for GFP (green) and OCT4 (magenta)
926 proteins, cyan and white arrowheads indicating $GFP^{+}OCT4^{+}$ and $GFP^{+}OCT4^{-}$ cells,
927 respectively. Epiblast (**e**) and allantois (**f**) are outlined. (**f**) 3D visualised images (see Methods).
928 Scale bar, 100μm.
929

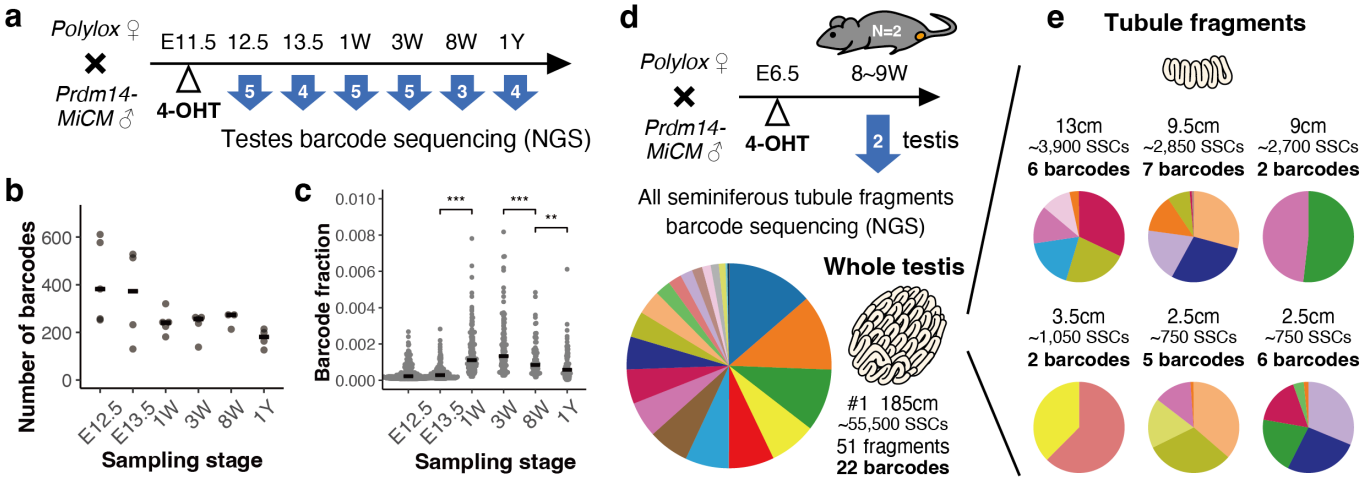

Figure 4. Barcode analysis after late induction and in fragments of seminiferous tubules

a, Experimental overview. *Prdm14-MiCM*;*Polylox* male embryos were barcoded at E11.5, whose barcodes in germline were analysed at the indicated time points from individuals of indicated numbers shown in arrows.

b, Barcode diversity found in individual mice. Horizontal bars indicate medians. No significant changes were detected between nearby stages (two-sided MWW).

c, The contribution of individual clonal barcodes (P_{gen}<0.00003) in all recombined barcodes recovered from each mouse. ***p<0.001, **p<0.01, two-sided MWW. Horizontal bars in (**b**) and (**c**) indicate medians.

d, Experimental overview is shown in top. Testis from each of the two adult *Prdm14-MiCM*;*Polylox* mice (8~9W old) induced at E6.5 were decapsulated to collect all the fragments of seminiferous tubules. Then, barcodes in all the dozens of collected fragments were read individually, compiled to reconstruct their composition over an entire testis, and summarized in a pie chart (see Method for detail).

e, Examples of long and short tubule fragments obtained in (**d**), with barcode reads therein. In (**d**) and (**e**), same colour among pie charts indicates same barcode. See Ext. Data Fig. 7 for full dataset for this and the second testis. Estimated SSC numbers in each fragment shown (see Methods).

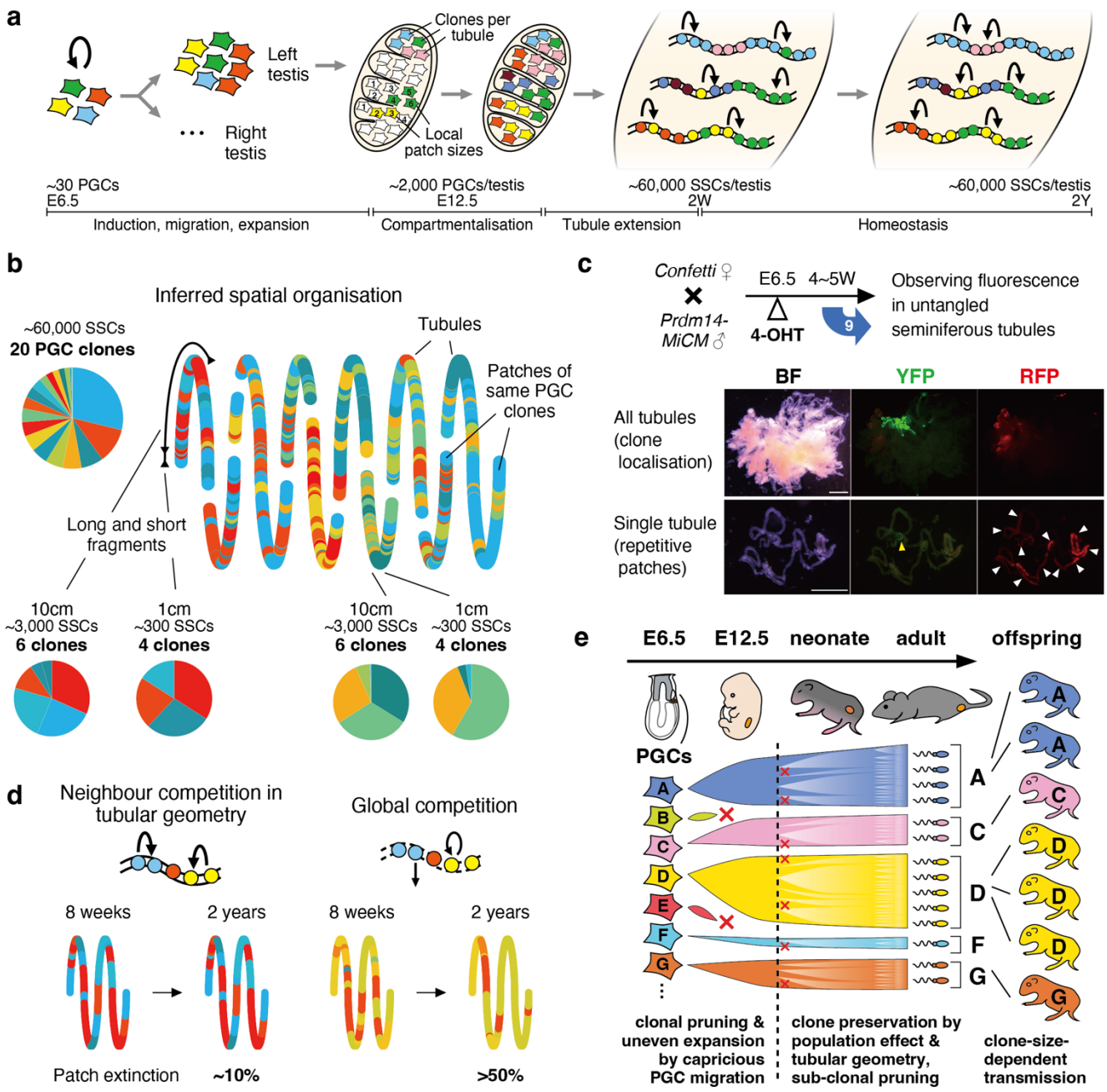

Figure 5. Modelling the lifetime clonal dynamics of male germline

a, Scheme for modelling the lifetime dynamics of the ~30 initial PGC clones at E6.5. Following the modelling over early phases till E12.5 (Fig. 3), additional models were developed to capture the germline fate behaviour over extended times, including the compartmentalisation into newly formed testis cords (E12.5), seminiferous tubule extension till 2W, and persistent homeostasis from 2W to 2Y of age. See Supplementary Methods in detail.

b, A typical example of the inferred spatial organisation of E6.5 PGC clones at 8 weeks after

958 birth, simulated using the sequential model summarized in (**a**). Within a single testis containing
959 ~60,000 SSCs, 20 PGC clones survived and were distributed across 11 separate tubule loops.
960 These clones were not evenly distributed; rather, each tubule loop harboured only a subset of
961 clones. The clones formed a mixed, repetitive patchwork structure in which short segments
962 contained a disproportionately large number of PGC clones (e.g., 4 clones in a 1-cm segment),
963 compared to long segments (e.g., 6 clones in a 10-cm segment), consistent with experimental
964 observations (Fig. 4d,e and Extended Data Fig. 7).
965 **c**, Visualization of PGC clone distribution using the *Confetti* multi-fluorescence lineage reporter.
966 Experimental design (top). Fluorescence images (middle and bottom) of gently untangled whole
967 seminiferous tubules from a single testis of a *Prdm14-MiCM;Confetti* mouse labelled at E6.5 (2-
968 3m Right), harbouring large YFP^+ and RFP^+ patches (middle), or a dissected tubule fragment (2-
969 3m tubule 4) containing a small YFP^+ patch and a cluster of non-contiguous RFP^+ patches,
970 indicated by yellow and white arrowheads, respectively (bottom). Scale bar, 2 mm.
971 **d**, Model prediction of the lifetime dynamics of local patches under different modes of adult
972 homeostatic regulation. In the neighbour competition model (left), which incorporates the
973 geometry of seminiferous tubules, local patch lengths remain highly stable with a minimal patch
974 extinction over 2 years life span. In contrast, a hypothetical global competition model with the
975 same differentiation output but agnostic of spatial geometry (right) shows a pronounced
976 disintegration of the local patch structure.
977 **e**, A schematic diagram summarizing the clonal dynamics of mouse male germline from
978 development to the next generation.
979

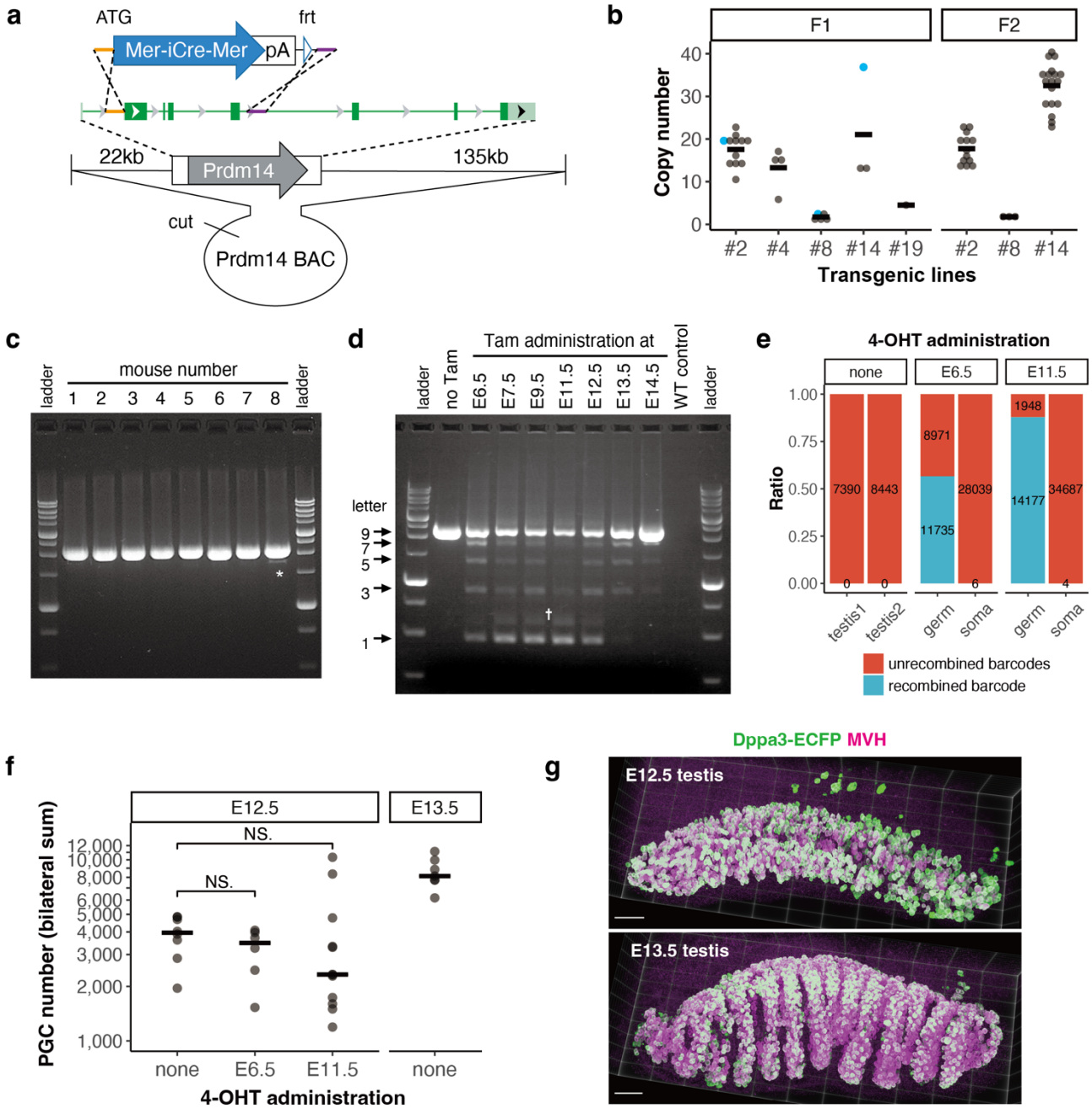

Extended Data Figure 1. Generation of *Prdm14-MiCM* transgenic alleles

a, Design of the *Prdm14-MiCM* BAC plasmid used for generating the *Prdm14-MiCM* transgenic allele, in which exons 2 to 5 was replaced by *Mer-iCre-Mer* CDS and a polyA (pA) addition signal.

b, Copy number of the *Prdm14-MiCM* transgene in independent multiple lines, measured by genomic qPCR. Horizontal bars indicate means. The F_1 individuals coloured in cyan were backcrossed to obtain the F_2 offspring. Given the largely unchanged copy number between F_1

988 and F_2 generation, these transgenes were highly expected to be integrated in a single locus in
989 lines #2, #8, and #14.
990 **c**, PCR-amplification of the *Polylox* locus from the tail DNA of *Prdm14-MiCM;Polylox* mice
991 with tamoxifen administration at E6.5, showing predominant amplification of 9-letter length
992 fragments. The lane with asterisk incudes a shorter amplified band (7-letters), likely due to a
993 leaky recombination in early embryos. 3 out of 74 mice (4%) with or without tamoxifen
994 administration showed such recombined short fragment(s) in tail DNA, which were excluded
995 from subsequent analyses.
996 **d**, Representative examples of the PCR-amplified barcode sequences from testes of 3-weeks-old
997 mice, which have received tamoxifen administration at different developmental time points as
998 indicated. The amplified fragments with five lengths, corresponding to the 9, 7, 5, 3, and 1
999 letters, indicate that homologous recombination occurred between the loxP sequences contained
1000 in the *Polylox* sequence, as expected. Consistent with the expression window of Prdm14[22],
1001 prominent recombination was observed between E6.5 and E13.5. Dagger indicates an
1002 unidentified fragment around 600bp, which were informatically excluded from the analysis.
1003 Mice that received no tamoxifen showed no evidence of barcode recombination.
1004 **e**, Verification of tamoxifen-dependent and germ cell-specific barcode induction. Testes from 3-
1005 weeks-old *Prdm14-MiCM*;*Polylox* mice without 4-OHT administration contained no
1006 recombined barcodes (left). The actual numbers of Sequel sequence reads are indicated on each
1007 coloured bar. *Prdm14-MiCM*;*Polylox;Dppa3-ECFP* triple transgenic embryos were induced by
1008 4-OHT administration to mothers at E6.5 or E11.5 (middle and right). Then, germ cells
1009 ($ECFP^+$) and gonadal somatic cells ($ECFP^-$) were FACS-sorted from pools of gonadal cell
1010 suspension prepared from eight E12.5 embryos obtained from a single litter (2 males and 6
1011 females for E6.5; 3 males and 5 females for E11.5). Recombined barcodes were detected
1012 exclusively in the germ cell fraction (i.e., PGCs), consolidating that recombined barcodes in
1013 gonads have derived specifically from germ cells in both sexes.
1014 **f**, The total number of PGCs (or gonocytes/prospermatogonia), summed from the bilateral testes
1015 of *Prdm14-MiCM*;*Polylox*;*Dppa3-ECFP* mice, at E12.5 (with or without 4-OHT
1016 administration) and E13.5 (without 4-OHT administration). PGCs were counted based on
1017 immunostaining of Dppa3-ECFP and DDX4, and image analysis of encircled nuclei (see
1018 Methods). Horizontal bars indicate medians. No statistical significance was detected (two-sided
1019 MWW).
1020 **g**, Three-dimensional representative images of E12.5 and E13.5 testes showing PGCs

1021 immunostained for Dppa3-ECFP and DDX4, visualised using ClearVolume[56]. Scale bar, 100
1022 μm.
1023
1024

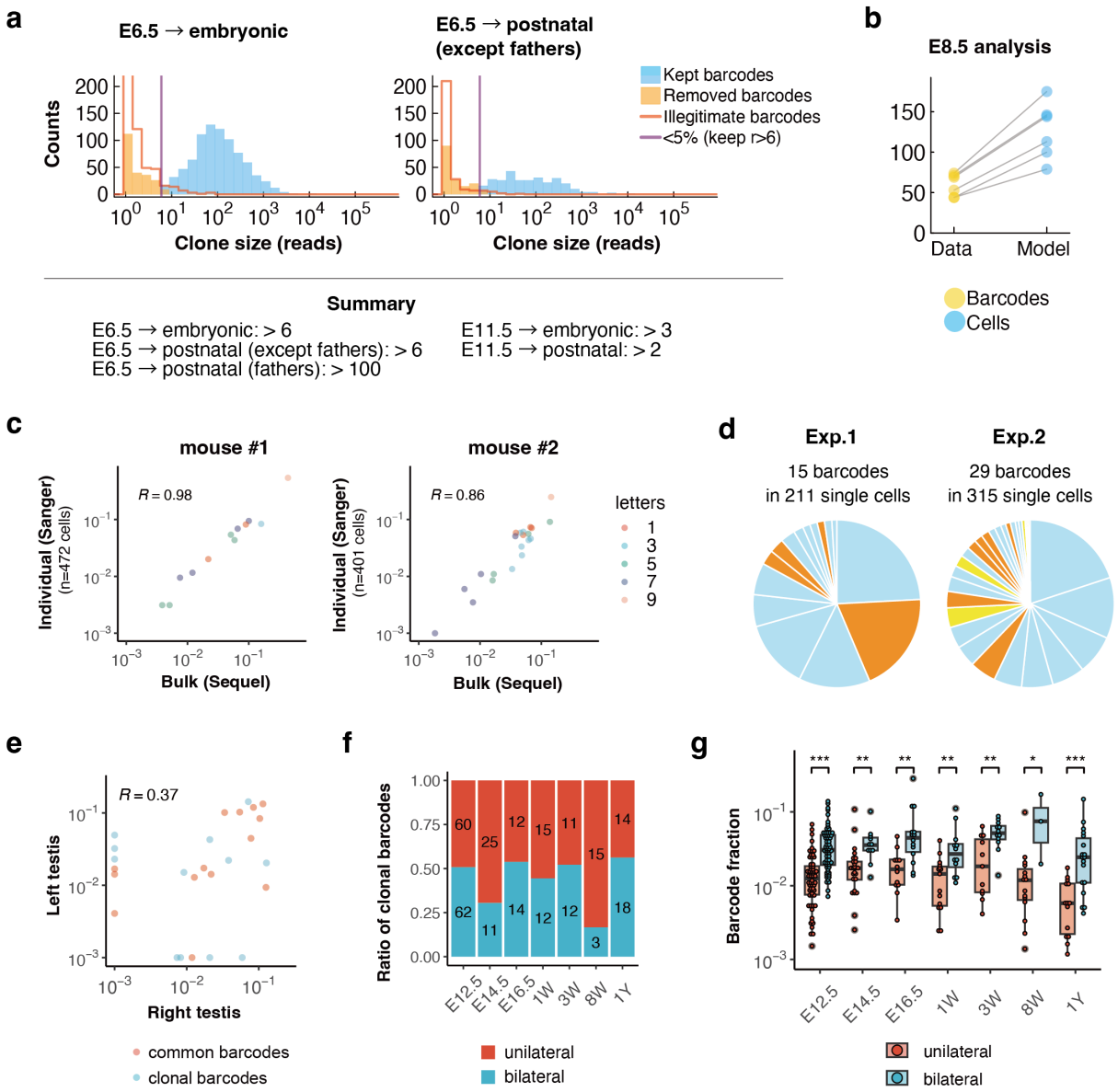

Extended Data Figure 2. Barcode analysis of E6.5-labeled PGC clones

a, Clone size (sequence read) distributions and criteria for barcode filtering. Barcodes were kept only if their clone size exceeded a defined threshold. The threshold (purple line) was set as the smallest clone size for which the number of remaining illegitimate barcodes (red) fell below 5% of the number of remaining legitimate barcodes (blue). Legitimate barcodes with clone sizes smaller than or equal to the threshold were excluded from subsequent analyses (orange).

b, Estimation of the cell number leading to the observed barcode outcomes, inferred from a model simulation with a given number of cells recombining their *Polylox* cassette intrinsically. The model was fitted to find the most probable cell number (blue) best explaining the unique

1035 barcodes observed in E8.5 PGCs, after induced at E6.5 (yellow).
1036 **c**, Validation of proportionality between the bulk barcode reads by amplicon sequencing using
1037 long-read sequencers (Sequel, Pacific Biosciences) and the actual composition of barcoded
1038 cells. A $CDH1^{+}/CD9^{+}/KIT^{-}$undifferentiated spermatogonia fraction (i.e., SSCs) were FACS-
1039 sorted from bilateral testes of two male mice, each barcoded at E6.5 and collected at 26 and 37
1040 weeks of ages. On one hand, the *Polylox* sequences contained in this fraction were read by a
1041 bulk amplicon sequencing using Sequel; in parallel the same cell fraction was further sorted into
1042 individual cells, whose barcodes were amplified and read by Sanger sequencing. As displayed,
1043 the results of bulk sequencing showed strong linear correlation with individual read, irrespective
1044 of the letter length as colour-indexed. 10^{-3} was added to each barcode's frequency for $\log_{10}$
1045 transformation; Spearman's rank correlation coefficients (R) are shown.
1046 **d**, Composition of barcodes induced at E6.5 and analysed in E13.5 testes, through Sanger-
1047 sequencing the individually sorted PGCs. Results from two independent experiments were
1048 shown, with clonal barcodes indicated (P_{gen}<0.001 and <0.0011, orange and yellow
1049 respectively). These results consolidate the conclusion based on the bulk sequencing that single
1050 PGC-derived clones induced at E6.5 unequally expand during their migratory stage.
1051 **e**, Barcode composition included in right and left testes, with common (P_{gen}≥0.001) and clonal
1052 (P_{gen}<0.001) barcodes coloured in red and cyan, respectively. Representative results from a
1053 single mouse (ID: m060) were shown. 10^{-3} was added to each barcode frequency for $\log_{10}$
1054 transformation; Spearman's rank correlation coefficient (R) is shown.
1055 **f**, Fractions of clonal barcodes observed unilaterally versus bilaterally, collected from all mice
1056 harvested after E12.5.
1057 **g**, Contributions of unilaterally versus bilaterally detected clonal barcodes in all recombined
1058 barcode reads. Note that bilaterally observed barcodes show significantly higher contributions at
1059 all time points. ***p<0.001, **p<0.01, *p<0.05, two-sided MWW.
1060

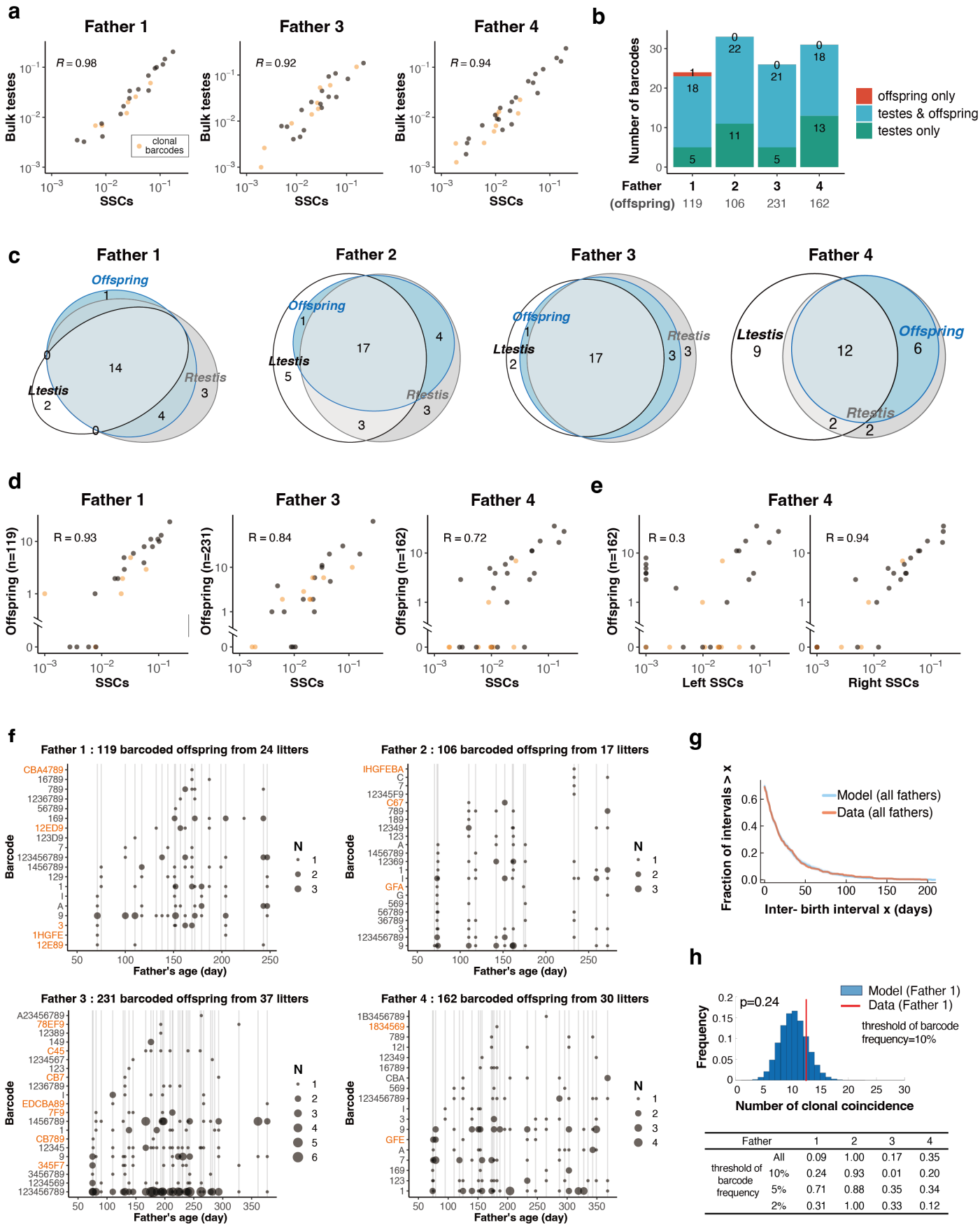

Father		1	2	3	4
threshold of barcode frequency	All	0.09	1.00	0.17	0.35
	10%	0.24	0.93	0.01	0.20
	5%	0.71	0.88	0.35	0.34
	2%	0.31	1.00	0.33	0.12

1062 **Extended Data Figure 3. Barcode transmission from SSCs through spermatogenesis to the**
1063 **offspring**
1064 Extended data for Fig. 2, involving four male mice barcoded at E6.5, mated with multiple
1065 females, and had their testes sampled at 1 year of age; followed by barcode reading in their
1066 SSCs, bulk testes, and offspring.
1067 **a**, Correlation between the barcode compositions in the SSCs and that in the bulk testes for
1068 three fathers but Father 2 presented in Fig. 2b. Note the similarly strong linear correlations. 10^{-3}
1069 was added to each barcode frequency for $\log_{10}$ transformation; Spearman's rank correlation
1070 coefficient (R) is shown.
1071 **b**, A bar plot showing diversity of barcodes appeared in fathers' testes only (green), both father's
1072 testes and offspring (cyan), and offspring only (red), summarized for each of the four fathers.
1073 All but 1 barcode identified in offspring were also found in the testes. The exceptional one
1074 likely derived from a PGC clone that became extinct before Father 1 reached one year of age.
1075 The number of offspring carrying barcodes are indicated below.
1076 **c**, Venn diagrams indicating barcode overlapping among the left testis (white), right testis (grey)
1077 and offspring (cyan), summarized for each father. Note that all barcodes that appeared in Father
1078 4's offspring were included in Father 4's right testis.
1079 **d**, Correlation between barcode composition in SSCs and in offspring, with the result from
1080 Father 2 shown in Fig. 2c. Note the similarly strong linear correlations. 10^{-3} was added to each
1081 barcode frequency for $\log_{10}$ transformation; Spearman's rank correlation coefficient (R) is
1082 shown.
1083 **e**, Correlation between barcodes found in SSCs from left or right testis of Father 4 and those
1084 observed in its offspring. Note that barcodes in offspring show strong correlation with SSCs
1085 from the right, but not the left, testis, suggesting that offspring of Father 4 originated
1086 exclusively from the right testis.
1087 **f**, Summary of the barcodes transmitted to offspring, plotted for the father's age on offspring's
1088 birthday. Grey vertical lines mark each litter's birthday; dots represent littermates whose size
1089 indicates the number of littermates sharing the same barcode. Clonal barcodes are coloured in
1090 orange.
1091 **g**, Analysis of inter-birth intervals in reference to a random-shuffle model. Inter-birth intervals
1092 were aggregated from each father, quantifying the time between births of pups with the same
1093 barcode. Interval times of zero arise from barcode coincidences in pups of the same litter. Model
1094 simulations were obtained by shuffling the barcodes of all pups for each father randomly, and

aggregating intervals as done for the data. Solid lines represent data (red) and the median of repeated model simulations (blue); band indicates 95% credibility region of the model. **h**, Probability of clonal coincidence, defined as offspring sharing the same barcodes in the same litter, were compared between model and data. The representative plot (top) shows the result using barcodes of Father 1 with frequency lower than 10%. Blue columns indicate the probabilities of the number of the clonal coincidence calculated by Monte Carlo samplings. Red lines indicate the actual number of clonal coincidences observed in the experiments. Probabilities based on different thresholds of barcode frequency are also shown (bottom table). These tests hardly showed statistical significance, consistent with the idea that each offspring was derived from PGC clones randomly selected from an SSC pool.

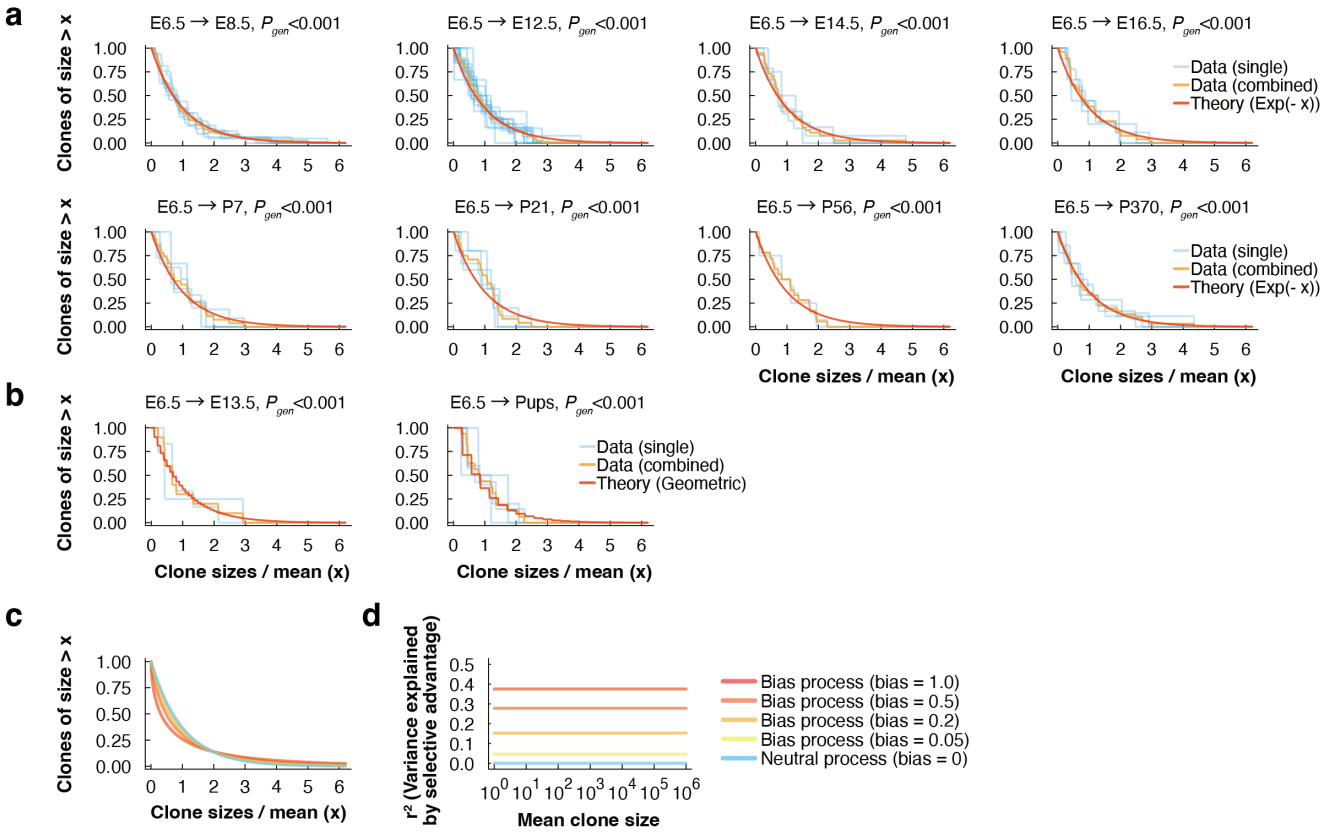

Extended Data Figure 4. Rescaled clone size distributions conforming with neutral birth-death processes

a, Size distributions of E6.5-barcoded PGC clones (i.e., read distribution of clonal barcodes with P_{gen}< 0.001) at indicated time points were rescaled by the mean value for each mouse (blue) and grouped mice (orange), and were compared to the theoretical distribution expected from a neutral birth-death process following the continuous scaling law of the exponential function (red; Supplementary Methods).

b, Size distribution of E6.5-induced PGC clones (with clonal barcodes) obtained from individual SSCs (analysed at E13.5) and from individual pups, compared to the theoretical distribution predicted by a discrete geometric model assuming neutral clonal competition.

c,**d**, Effect of clonal bias and persistent selective advantages on clone size distributions. Rescaled clone sizes (**c**) are compared between the neutral model (blue), assuming neutral clonal competition without bias (birth-death models; **a**,**b**), with non-neutral dynamics at various bias levels (yellow to red). The bias parameter b is defined as $\mathrm{CV}_{\mathrm{bias}} = (1 + b)\ \mathrm{CV}_{\mathrm{neutral}}$, i.e. enhancing the coefficient of variation (CV) of the neutral clone sizes. Levels of clonal bias correspond to a certain fraction of the clone size variability that is explained by selective

advantages between clones, as quantified by the squared correlation r^2 (**d**; Supplementary Methods). It holds that $r^2 = \big(b(b+2)\big)/\Big(2\big(1+(b(b+2))\big)\Big)$, for any mean clone size. The remaining fraction of the clone size variability, $1 - r^2$, originates from neutral stochasticity. Clone size variability for $b = 0.2$ already deviates noticeably from the neutral case (**c**) and the data (**a**,**b**), indicating that PGC clone size variability is, by and large, driven by neutral stochastic effects (i.e., 85% - 100%).

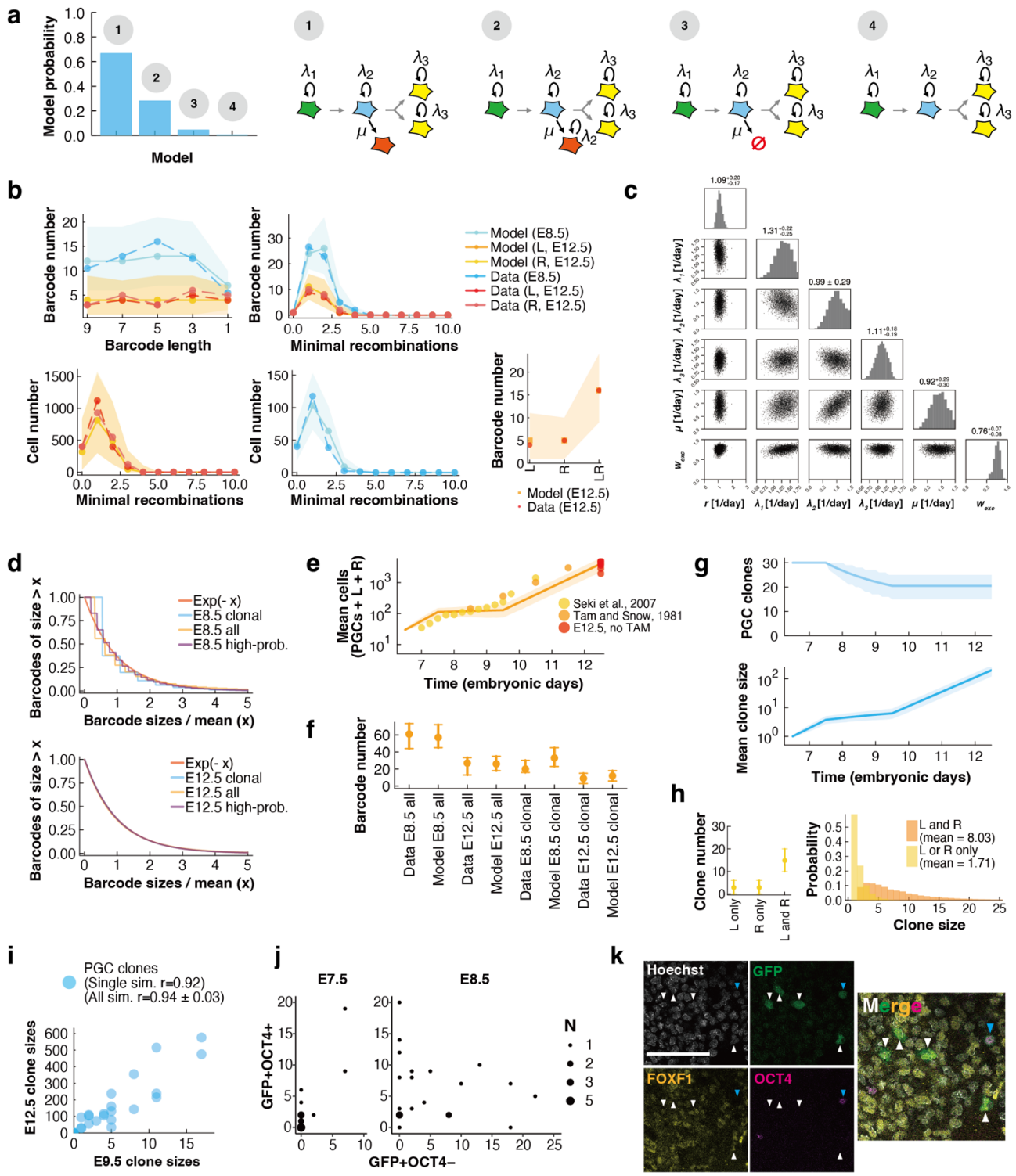

Extended Data Figure 5. Modelling the clonal dynamics of PGCs from E6.5 to E12.5

a, Posterior probabilities (left) inferred for the four tested modelling schemes (1-4; right). All models simulate PGC clonal dynamics in three sequential phases of birth-death processes from E6.5 to E7.5 (green), E7.5 to E9.5 (blue) and, after splitting into left and right gonads, from

1135 E9.5 to E12.5 (yellow), following the respective division rates (λ_1, λ_2 and λ_3). The top model (1)
1136 simulates PGC loss with a rate μ from the second-phase PGCs (blue) into a non-arriving PGC
1137 fraction (red) that is still measured at E8.5 but does not proliferate and does not reach the
1138 gonads (yellow). Model 2 is like model 1, except that the non-arriving PGC fraction continues
1139 to divide with the same rate. Model 3 simulates PGC loss as immediate cell death. The model
1140 (4) which assumed all PGCs to survive without loss showed the lowest predictive capacity.
1141 **b**, Barcode and clonal dynamics statistics used for the inference. Posterior statistics of the top
1142 model (Model 1 in (**a**)) are shown with 95% credibility bands, compared to the data as
1143 indicated.
1144 **c**, Posterior parameter distributions as inferred from the data for the top model. The set contains
1145 biological parameters specifying PGC division and loss (λ_1, λ_2, λ_3 and μ), and technical
1146 parameters specifying the *Polylox* recombination kinetics (recombination rate r and excision
1147 bias w_{exc}).
1148 **d**, Predicted distribution of *Polylox* barcode contribution simulated for E8.5 and E12.5 (top
1149 model with posterior parameters), rescaled with their means, based on clonal (blue), non-
1150 clonal/high-probability (purple) and all (orange) barcodes. In comparison, the theoretical scaling
1151 law of birth-death process (red) was indicated. The discreteness in E8.5 barcode sizes (upper
1152 panel) comes from the low cell numbers at this time point. Note the good agreement with the
1153 data, as shown in Extended Data Fig. 4 for clonal barcodes.
1154 **e**, Predicted germ cell numbers (excluding non-arriving PGCs), shown as mean (lines) with
1155 95% credibility bands. As reference, experimental measurements of embryonic PGC numbers
1156 are indicated (dot; see also Extended Data Fig. 1f).
1157 **f**, Prediction of the total and clonal *Polylox* barcode numbers at E8.5 and E12.5 inferred by the
1158 top model, compared with the observed data. Median number (dot) with 5th and 95th percentiles
1159 (error bars) are shown. Note that the number of all barcodes is fitted in (**b**), but the clonal
1160 barcode numbers are a model prediction.
1161 **g**, Prediction of the clone dynamics originated from E6.5 PGCs based on the top model with
1162 inferred parameters. Number of surviving E6.5 PGC-derived clones (top) and mean clone sizes
1163 of surviving E6.5 PGC-derived clones (bottom). Both model predictions (lines) are shown with
1164 95% credibility bands.
1165 **h**, Predicted number and size distribution of clones originating from the initial ~30 PGCs at
1166 E6.5, which arrived at the left (L) and/or right (R) gonads at E9.5, based on the top model with
1167 inferred parameters. Median clone number (dot) with 2.5^{th} and 97.5^{th} percentiles (error bars).

The model predicts that left-right shared clones are bigger E9.5 and in the long terms, consistent with the experimental data (see also Fig. 3b, Extended Data Fig. 2g).

i, Correlation between the predicted clone sizes of the same clones between E9.5 and E12.5; a representative simulation (sim.) shown, correlation values indicated for the single and all simulations.

j, The numbers of $GFP^{+}OCT4^{+}$ and $GFP^{+}OCT4^{-}$ cells in E7.5 (left) and E8.5 (right) embryos. Dot size indicates the number of embryos with the same cell counts.

k, Representative images of E8.5 allantois stained for GFP, OCT4, and FOXF. A significant portion of $GFP^{+}OCT4^{-}$ cells at E8.5 were positive for FOXF1, a marker of extraembryonic mesoderm including allantois[31] (white arrowheads). Scale bar, 100μm.

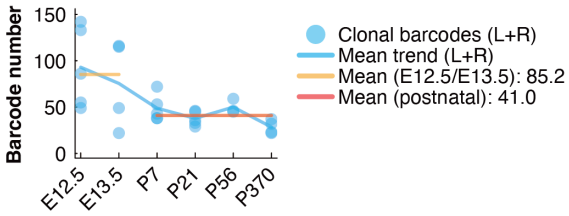

Extended Data Figure 6. Estimating the survival chance of single E11.5/E12.5 PGC-derived clones

Number of clonal barcodes (P_{gen}<0.00003; left and right testes combined) induced at E11.5 and recovered over embryonic and postnatal stages as indicated. The reduction in the mean number of clonal barcodes (horizontal lines) from ~85 in E12.5–13.5 to ~41 after birth indicates that the survival chance of a single PGC-derived clone from E12.5 to adult stages is approximately 50%. See Fig. 4b for total barcode numbers.

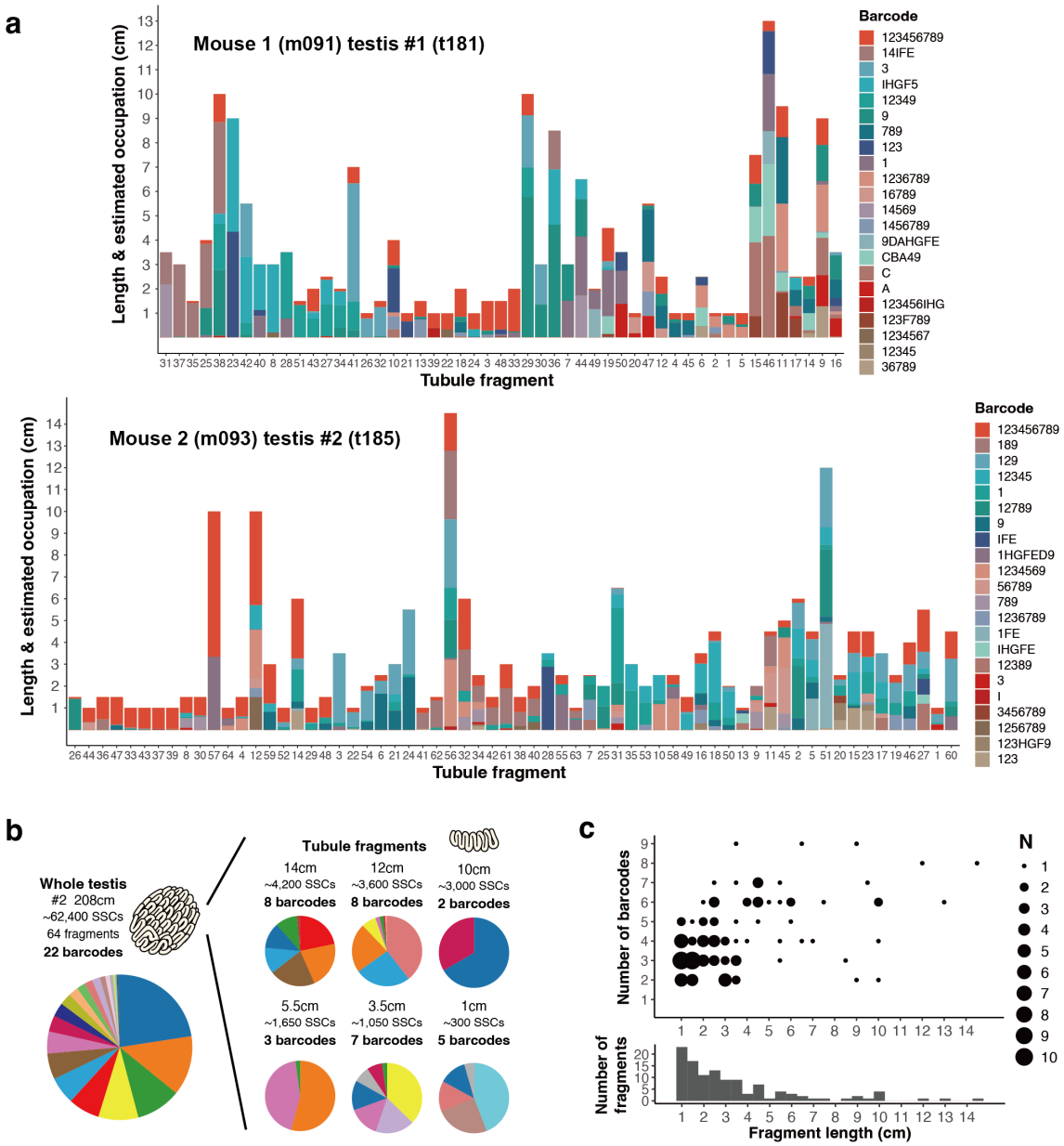
a
Mouse 1 (m091) testis #1 (t181)
Length & estimated occupation (cm)
Tubule fragment
Barcode
123456789
14IFE
3
IHGF5
12349
9
789
123
1
1236789
16789
14569
1456789
9DAHGFE
CBA49
C
A
123456IHG
123F789
1234567
12345
36789
Mouse 2 (m093) testis #2 (t185)
Length & estimated occupation (cm)
Tubule fragment
Barcode
123456789
189
129
12345
1
12789
9
IFE
1HGFED9
1234569
56789
789
1236789
1FE
IHGFE
12389
3
I
3456789
1256789
123HGF9
123
b
Whole testis
#2 208cm
~62,400 SSCs
64 fragments
22 barcodes
Tubule fragments
14cm
~4,200 SSCs
8 barcodes
12cm
~3,600 SSCs
8 barcodes
10cm
~3,000 SSCs
2 barcodes
5.5cm
~1,650 SSCs
3 barcodes
3.5cm
~1,050 SSCs
7 barcodes
1cm
~300 SSCs
5 barcodes
c
Number of barcodes
Number of fragments
Fragment length (cm)
N
d
Fragment 11
Fragment 29
Fragment 38
Fragment 46
Fragment 9
Fragment 15
Fragment 23
Fragment 36
Fragment 41
Length (cm)
Subfragment
Barcode

Extended Data Figure 7. Barcode distribution over the seminiferous tubules in the adult testis

a, Summary of two sets of barcode reads, each obtained from seminiferous tubule fragments representing a whole single testis each, separately sampled from two different individuals that were barcoded at E6.5 and sampled in 8 (Mouse 1) and 9 (Mouse 2) weeks of age. Each column represents the set of barcodes observed in a single fragment of the indicated length, colour-coded according to the identity and composition of barcodes, as specified on the right. Fragments are aligned on the x-axis according to hierarchical clustering of barcode frequency.

b, Summary of the uneven barcode distribution of the testis #2 from Mouse 2, presented in a same manner with Fig. 4d,e.

c, Number of barcodes detected in each fragment with different lengths (shown at the bottom). Data from the two testes (#1 and #2) are combined. Dot size indicates the number of fragments with the same length and barcode count.

d, Barcode compositions in long contigs of tubule fragments obtained from testis #1 of Mouse 1, analysed separately in their sub-fragments. Sub-fragments are numbered in spatial sequence, except for the branched fragment (#46). Each column depicts each sub-fragment, with the total heights reflecting the tubule lengths and colours indicating the barcode identities (specified for each panel).

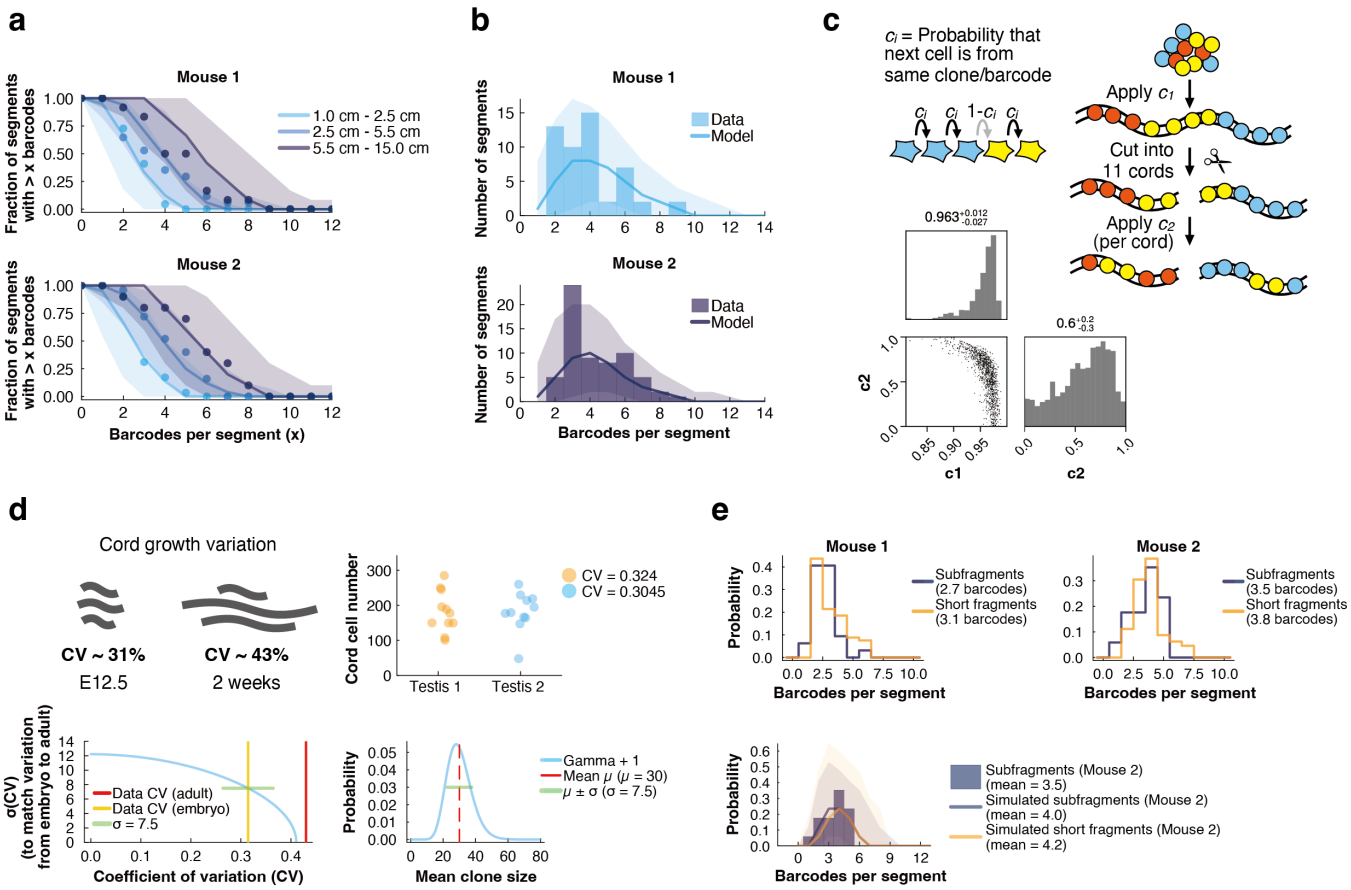

Extended Data Figure 8. Inference of a model for tubular PGC dynamics

Setup and inference of a model extending the PGC clone dynamics after E9.5, including phases of testis cord formation at ~E12.5, their expansion (E12.5 to 2 weeks), followed by homeostasis as analysed experimentally at 8 weeks.

a, Statistics used for the model inference. Distributions of *Polylox* barcode number included in tubule segments (Extended Data Fig. 7) were fitted simultaneously for three categories based on the indicated segment lengths for each of the two testes from two mice analysed (barcoded at E6.5, simulated until 8 weeks after birth). Data (dots) and posterior model inference (solid lines with 95% credibility bands) shown.

b, Predictive capacity of the model validated in term of the distribution of barcode numbers across all analysed segments (data not directly used for fitting). Data (histograms) and the model prediction (solid line with 95% credibility bands) are overlayed.

c, Model setting of distributing the PGC clones upon compartmentalisation through testis cord formation at E12.5. The parameters c_1 and c_2 model the spatial distribution of clones on the forming ~11 tubule loops (effectively one-dimensional) at E12.5. Both parameters measure how

strongly cells of the same clone form local clusters (top schemes). The first parameter c_1 controls the cluster sizes of clones within a cord at the time of compartmentalisation, and with that, the number of clones per cord. When PGCs subsequently align into the one-dimensional tubular arrangement, clusters may mix and yield the final organisation of local patches. The sizes of these local patches are controlled by the second parameter c_2 acting on the cluster sizes. Inferred posterior model parameters c_1 and c_2 (lower left).

d, Prediction of the variation in the extension of testis cords/seminiferous tubules within a single testis between E12.5 and 2W after birth. Summary of the coefficient of variation (CV) of cord cell numbers at E12.5 and in 2W after birth (top left), based on our measurement (see the top right panel) and Nakata et al., 2015[38], respectively. Numbers of germ cells included in individual testis cords of two E13.5 testes, with respective CVs indicated (top right). Shown values were rescaled to match the total germ cell number at E12.5 (~2,000) using E13.5 data (Extended Data Fig. 1f,g**)** as a close approximation. Inferring the cord variation parameter σ (i.e., the variability of extension of individual testis cords/seminiferous tubules within a single testis between E12.5 to 2W; bottom left). The blue line indicates the required heterogeneity to increase the initial embryonic CV to the adult CV during expansion. Best prediction of the 2W value from of the E12.5 value is given with $\sigma \approx 7.5$. (see Supplementary Methods). A gamma distribution was employed to simulate cord growth with the inferred cord variation parameter of $\sigma \approx 7.5$ (Bottom right).

e, Validation of our modelling scheme of heterogeneous extension of testis cords/seminiferous tubules (with $\sigma \approx 7.5$) by independent, barcodes-based data. Heterogeneous cord expansion (as specified by CVs in (**d**)) predicts a shift in the mean barcode number between short fragments and sub-fragments (pieces of a long fragment) when accounting for an identical underlying fragment length distribution. Data (top panels; means indicated in legend) show a slight shift of ~0.3 barcodes, consistent with the model prediction (lower panel) by ~0.2 barcodes (see Supplementary Methods for more details).

a

mouse_ID	day_old	Ltestis_color	Rtestis_color
1-1m	29	-	Y
1-2m	31	-	-
1-3m	31	-	-
2-1m	30	Y	RY
2-2m	35	-	Y
2-3m	35	RY	RY
3-2m	30	-	Y
3-3m	36	-	-
3-4m	36	-	-

b

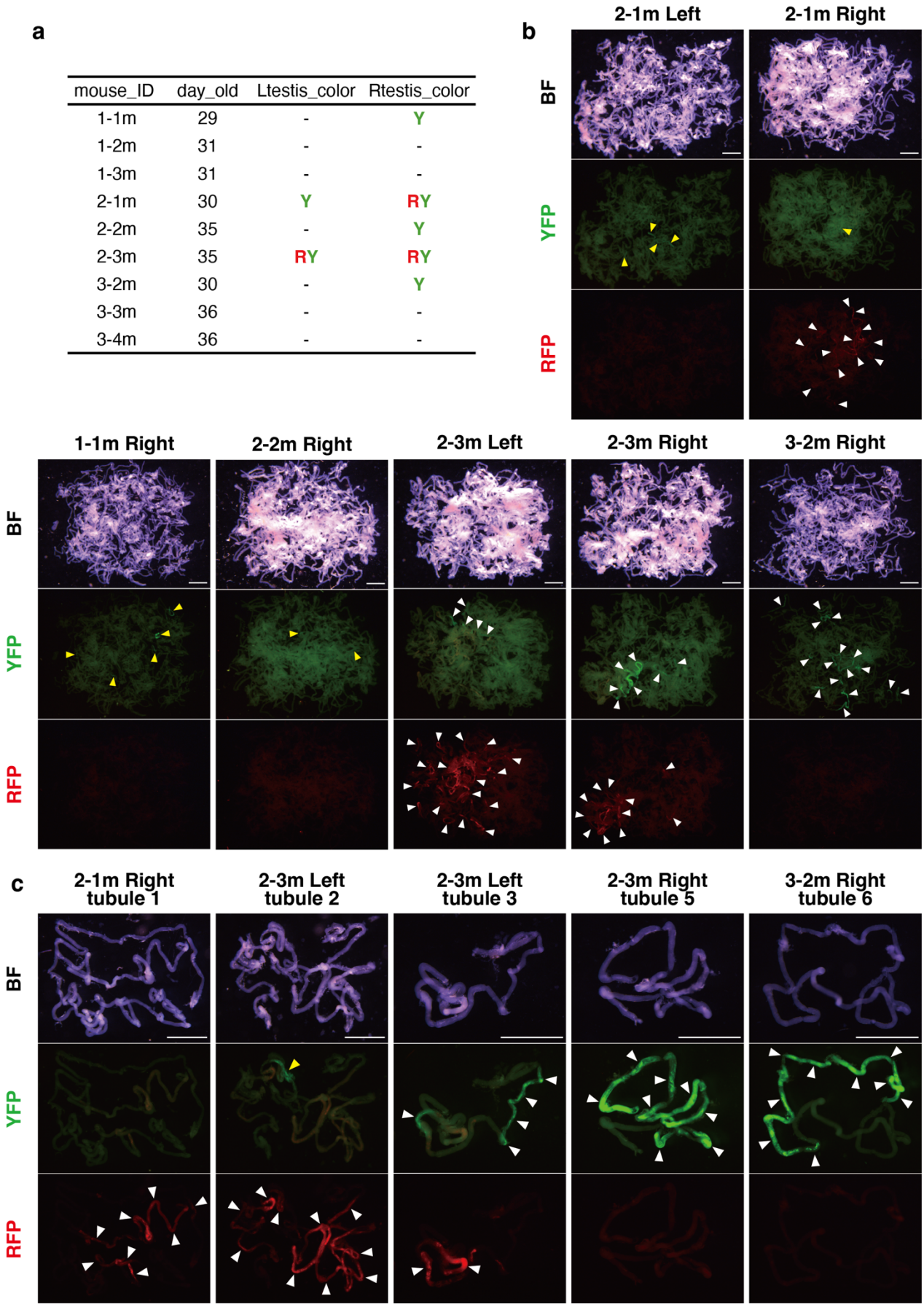

1253 **Extended Data Figure 9. Visualization of E6.5 PGC-derived clones in adult using *Confetti***
1254 **reporter, related to Fig. 5c**
1255 Following the experimental design presented in Fig. 5c top panel, PGCs were sparsely labelled
1256 at E6.5 and their clones were visualised at 4-5W after birth.
1257 **a**, Summary of the analysed nine *Prdm14-MiCM*;*Confetti* mice and their fluorescent cells in
1258 their testes. R and Y indicate cRFP and cYFP, respectively. Note that only 5 in 9 mice contained
1259 fluorescent cells, and 4 of them having colours found only in unilateral testis, suggesting highly
1260 oligo-clonal labelling. mCFP and nGFP patches were not observed.
1261 **b**, Thoroughly disentangled whole seminiferous tubules in testes of *Prdm14-MiCM*;*Confetti*
1262 mice. Seven testes in (**a**), which included one or more fluorescent-labelled patches are shown.
1263 Note the prominent green patches in 2-3m Left, 2-3m Right, and 3-2m Right, and red patches in
1264 2-1m Right, 2-3m Left, and 2-3m Right testes (white arrowheads). Small green patches are also
1265 found, obscured by background signals in 1-1m, 2-1m and 2-2m (yellow arrowheads).
1266 **c**, Higher magnification views of isolated fragments of seminiferous tubules carrying patches of
1267 fluorescence-labelled cells prepared from the indicated testes. Note prominent and extended
1268 green and red patches in tubules 3, 5, 6 and tubules 1, 2, 3, respectively (white arrowheads), and
1269 small green patches in tubules 2 (yellow arrowhead). Scale bar, 2mm.
1270

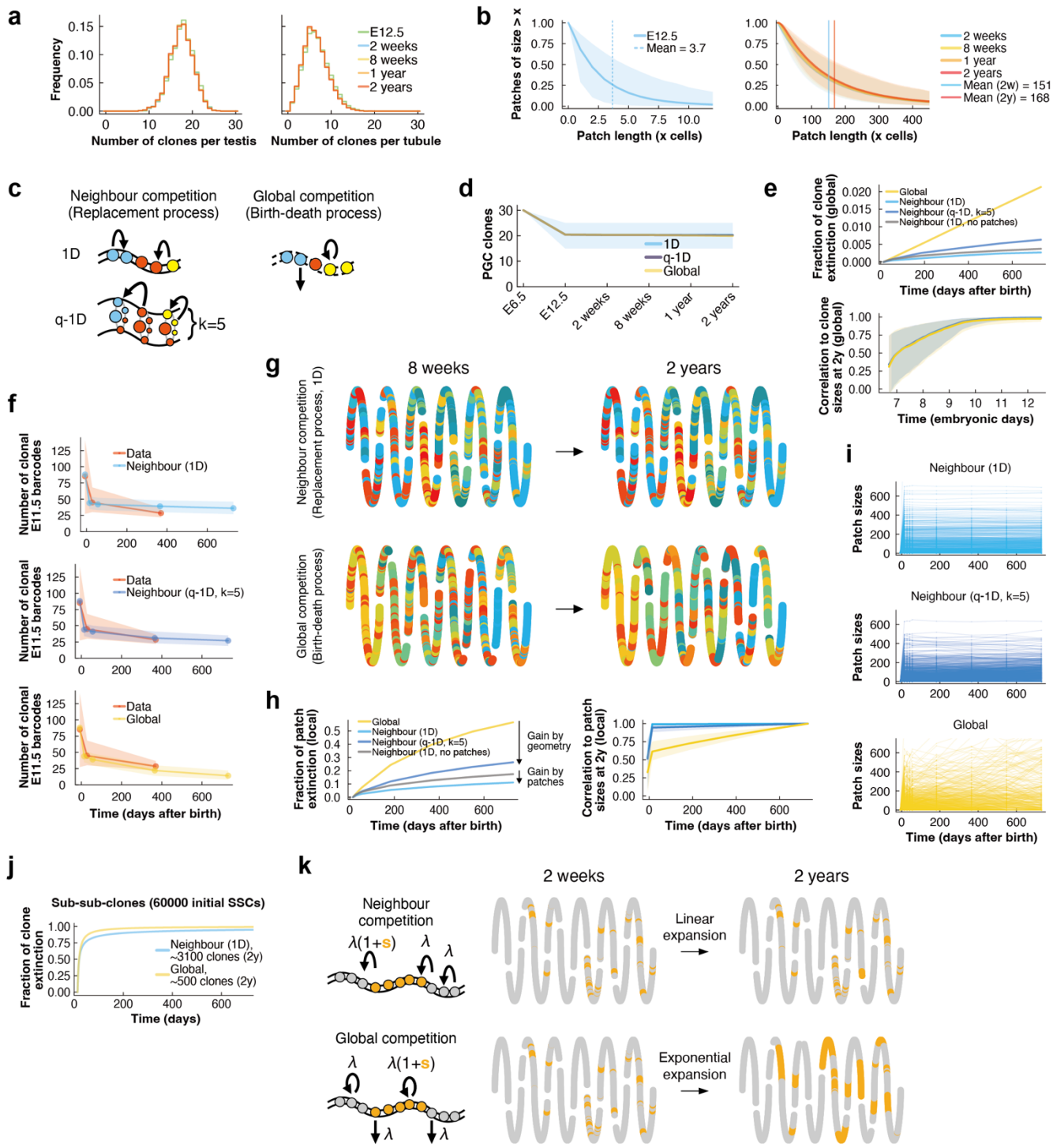

Extended Data Figure 10. Inferred spatiotemporal dynamics of PGC clones over the male life span

Lifelong dynamics of male germline clones (instead of *Polylox* barcodes) from their emergence at E6.5 to 2 years of age were inferred both globally (averaged over an entire testis) and locally

(considering spatial organisation within seminiferous tubules). The integrative model consists of a sequence encompassing early clonal dynamics from E6.5 to E12.5, the formation and elongation of testis cords/seminiferous tubules by 2 weeks after birth, and an extended homeostatic phase lasting up to 2 years of age.

a, Model prediction for the number of surviving PGC clones within one testis (left) and within one of the ~11 testis cords/seminiferous tubules (right), at different time points.

b, Model prediction of patch size distributions at E12.5 (left) and at multiple postnatal time points (right). Median prediction (solid lines) and 95% credibility band are shown, with mean patch sizes indicated by vertical lines. Homeostatic phase was modelled under neighbour competition dynamic within one-dimensional tubules.

c, Schemes of regulation modes during the adult homeostatic phase. Neighbour competition in tubules is compared to a hypothetical global competition model as reference, to investigate the effect of the tubular geometry on clone and patch size dynamics. In the scheme of neighbour competition (left), a lost stem cell through differentiation is replaced by one of the neighbours to maintain a constant stem cell pool. A one-dimensional (1D) geometry (left top), in which a lost stem cell is replenished by duplication of either the left or right neighbour. A quasi-one-dimensional (q-1D) tubular configuration (left bottom) with k=5 cells in the circumference (based on Klein et al., 2010[37]), in which a lost stem cells is replenished by duplication of any one of the 4 neighbours (left, right, bottom or top). In the hypothetical global competition mode (right; modelled as a critical birth-death process), stem cell loss and duplication occur stochastically and without spatial coupling, while maintaining a balanced total number of SSCs.

d, Model prediction for the number of surviving E6.5 PGCs (starting from ~30) up to 2 years (solid lines; 95% credibility band for 1D). Note that after E12.5, global PGC clones become very stable, in line with the observed *Polylox* barcodes induced at E6.5 (Fig. 1). Clone stability across the testis is robust, independent of the mode of adult homeostatic regulation (shown in (**c**)). Detailed dynamics for the early phase (E6.5 to E12.5) are shown in Extended Data Fig. 5g.

e, Model prediction for extinction probabilities and size correlation of global PGC clones following different modes of homeostatic regulation shown in (**c**). Over the testis wide, PGC clones show high stability from as early as ~E11, as indexed by low extinction during postnatal phase (top) and high correlation to their long-term clone sizes at 2 years (bottom), with the neighbour competition modes showing higher stability. Model bands show 95% credibility regions.

f, Projection of the model dynamics by following the E12.5 germ cell-derived clones (PGC sub-

clones) for their survival over time (compared for the three homeostatic regulation modes) with those observed in the E11.5 barcoding data (clonal barcodes, P_{gen}<0.00003). The q-1D setup in the neighbouring competition yielded the highest predictive power, likely due to the markedly smaller size of E12.5 germ cell-derived clones compared to those from E6.5 PGCs. Data and model bands show 95% credibility.

g, Model prediction of the spatial organisation of PGC clones in postnatal seminiferous tubules of a single testis from 8 weeks to 2 years of age, under different homeostatic regulation either by neighbour competition within tubules (upper panels) or by a hypothetical global competition as a reference (lower panels). In both scenarios, the testis is modelled as comprising 11 separate tubule loops, which contain a one-dimensional array of ~60,000 SSCs in total colour-coded by PGC clone identity (one of the ~30 initial clones). Cells belonging to the same clone (indicated by the same colour) often appear repeatedly as separate patches, within and across the tubule loops. Note the spatial organisation of such patches is high stable under neighbour competition, but unstable under a global competition.

h, Model prediction for extinction probabilities and size correlation of local patches, following different modes of homeostatic regulation shown in (**c**). The high stability of the neighbour competition dynamics is more clearly underscored by the fates of local patches, as evidenced by the extinction rates (left) and correlations with long-term patch sizes (right). Model bands show 95% credibility regions.

i, Model simulations of individual patch sizes over a testis, comparing different modes of homeostatic regulation. Note that global competition (birth-death process) shows lower stabilities as well.

j, Model prediction for the fraction of extinction of single SSC-derived clones (PGC sub-sub-clones) during homeostasis from 2 weeks to 2 years postnatally, comparing neighbour competition in a 1D tubular geometry with global competition. Neighbour competition maintains a higher clonal diversity after 2 years (indicated in legend), starting with ~60,000 SSC clones at 2 weeks.

k, Model prediction for the expansion of a single E6.5 PGC clone with a selective advantage during postnatal homeostasis, comparing neighbour competition in a 1D tubular geometry (top) with global competition (bottom). An identical clonal arrangement at 2 weeks (left) was simulated up until 2 years (right). The selected clone (orange patches) was equipped with an advantage of $s = 1\%$, increasing the rate of cell division (λ) in contrast to neutral PGC clones (all shown in grey). Under neighbour competition, enabled by the tubular geometry, the selected

1342 clone was effectively confined; in contrast, the clone expanded exponentially under the
1343 hypothetical global competition (Supplementary Methods).

Supplementary Information

The methods and theory for modelling germline clonal dynamics are detailed in the following sections *1. Supplementary Methods* and *2. Supplementary Equations*.

1. Supplementary Methods

Scaling of clone size distributions. We assessed whether clone sizes from E6.5&6.75 PGC barcoding conform with a neutral birth-death process; the theoretical basis for this procedure is given in Supplementary Equations a. We first applied the read threshold to filter spurious barcodes and subtracted the threshold from the kept clone sizes, so that the smallest possible clone size is again at one read (this mitigates censoring effects). Afterwards extant clone sizes were rescaled (divided) by their mean clone size, and the complementary cumulative probability distribution of the rescaled clone sizes was compared to the theoretical scaling law (Extended Data Fig. 4a,b). Further, this scaling of neutral clonal competition was compared to processes with inherent and persistent clonal biases (i.e., selective advantages) among the PGC clones at E6.5, confirming neutral stochasticity as the principal source underlying the observed clone size variation (Extended Data Fig. 4c,d; Supplementary Equations b).

Mechanics of *Polylox* recombination. *Polylox* barcode recombination was modelled as a Markov process in continuous time, each cell being subjected to a recombination rate r. We assumed this rate is the same for all cells during the entire recombination window; particularly, independent of the current barcode state. *Polylox* recombination was then simulated stochastically by starting all cells with the unrecombined barcode '123456789', selecting the next cell and time to recombine, conducting a recombination (that is, changing the cell's barcode state) and continuing this procedure until the end of the recombination window. The new barcode state was sampled from a 1,866,890×1,866,890 transition matrix specifying all legitimate *Polylox* recombinations[12]. Matrix values were assumed to be uniform, apart from a bias $w_{\mathrm{exc}} \in (0, 1)$ that tunes chances of excisions vs. inversions. For example, barcode '123456789' has 45 possible recombinations, 25 inversions (preserving barcode length 9) with probabilities $c\ (1 - w_{\mathrm{exc}})$ each and 20 excisions (leading to lengths 7, 5, 3 or 1) with probabilities $c\, w_{\mathrm{exc}}$ each, and $c = 1/(25\ (1 - w_{\mathrm{exc}}) + 20\ w_{\mathrm{exc}})$. Where applicable, such barcode recombination was tied to other reactions of cellular dynamics (cell division, loss, etc.) in a single model (see subsequent sections). At divisions, both daughter cells inherited the barcode of the mother.

Modelling PGC dynamics from E6.5 to E12.5. To infer the lifetime clonal dynamics of the ~30 PGCs induced at E6.5, we set up model inferences drawing from multiple barcoding experiments, starting with analysis stages E8.5 and E12.5. We reasoned that the accurate evolution of clonal loss and clone sizes are revealed from such a time-series inference, in contrast to single snapshots alone. Further, we designed the approach to be capable to switch between *Polylox* barcodes (introduced in a more continuous time window from E6.5 to ~E8.0) and clones derived from single E6.5 PGCs.

First, we created four models of clonal PGC dynamics spanning from E6.5 to E12.5 as continuous time Markov jump process with sequential phases of neutral birth-death processes (as tested in section 'Scaling of clone size distributions'). All models were initialized with thirty PGC clones at E6.5 that proliferated as a pure birth process with division rate λ_1 until E7.5, and continued to divide during a subsequent migration phase with rate λ_2 until E9.5. At E9.5 cells were randomly distributed to two compartments, representing left and right gonads (later testes), where they proliferated with rates λ_3 until E12.5. The models differ in their potential PGC loss during the migration phase (Extended Data Fig. 5a). In model 1, PGCs were lost with a rate μ to a non-arriving PGC fraction that was not distributed to the gonads at E9.5.

Second, we added *Polylox* barcodes to these models. Each cell was equipped with an internal barcode state, starting with the unrecombined barcode '123456789' in all cells at E6.5. Alongside the cellular dynamics, cells internally recombined their *Polylox* barcode with a rate r and excision bias w_{exc} from E6.5 to E8.0 (see section 'Mechanics of *Polylox* recombination'); after E8.0, barcodes were considered stable. Hence, given values for its biological parameters (λ_1, λ_2, λ_3 and μ), each model simulated specific E6.5 PGC dynamics. And, given additional values for the recombination parameters (r and w_{exc}), these PGC dynamics were simultaneously probed with *Polylox* barcodes, keeping track of barcode identities for all cells during the simulation.

These models were applied to *Polylox* barcoding data, using Bayesian parameter inference and model selection from ABCdeZ.jl. We compared data and models via summary statistics, iterating over many different parameter combinations. Flat priors were chosen: pure birth rates λ_1 and λ_3 uniform in $[0.5, 1.75]$ (per day), the migration parameters λ_2 and μ uniform in $[0, 1.5]$ (per day), the recombination rate r uniform in $[0, 3]$ (per day) and the excision bias w_{exc} uniform in $(0, 1)$. Summary statistics for the data were computed as median over all 6 and 13 mice for E8.5 and E12.5 analyses, respectively. A first set of summary statistics informed about clonal diversity, using distributions of *Polylox* barcode number (all barcodes used, no P_{gen} cutoff) over barcode lengths (9, 7, 5, 3, 1) and minimal recombinations (0, 1, …, 11), and sharing of

barcodes between left and right gonads (E12.5 only). A second set of summary statistics informed about total PGC cell numbers[23,24], using read distributions over barcode lengths and minimal recombinations rescaled to 200 (E8.5) and 2000 cells (E12.5 for left and right each). For each parameter set, models were simulated once until E8.5 and once until E12.5, producing analogue model summary statistics from simulated *Polylox* barcodes. The arriving and non-arriving PGC fractions were merged for the E8.5 readout if applicable (models 1 and 2). After fitting each model to the data, posterior model probabilities were obtained, and within each model, posterior parameter distributions.

To extrapolate to the clonal dynamics of the initial ~30 PGCs, the top model (model 1) was re-simulated with median values of the biological parameter posteriors, keeping track of the founding E6.5 PGC clones (instead of *Polylox* barcodes) for all cells during the simulation.

Clone initiating cell numbers for E8.5 analysis. We fitted a recombination-only model to observed barcode numbers of E8.5 analysis after E6.5&6.75 PGC barcoding, to assess whether inferred cell numbers conform with the PGC numbers in the recombination window (E6.5 to ~E8.0). The barcode data of each of the six mice (E8.5 analysis) was transformed to summary statistics of absolute barcode number distributions over *Polylox* barcode length (9, 7, 5, 3, 1) and minimal recombination number (0, 1, …, 10). For each mouse, the recombination model was fitted to these data, producing the respective summary statistics from simulations of *Polylox* barcode recombination in N cells at a recombination rate r. Prior distributions were uniform on intervals $N \in \{1, \dots, 500\}$ and $r \in [0, 4]$ (per day); the recombination window was fixed to 1.5 days and excision bias to 75% (as inferred from the PGC E6.5 to E12.5 dynamics). The median of the posterior distribution for N was reported as most likely cell number.

Spatial and lifetime model of PGC clonal dynamics. We extended the clonal PGC dynamics inferred during embryonic development (Fig. 3, section 'Modelling PGC dynamics from E6.5 to E12.5') in two aspects. First, starting around E12.5, PGCs in the gonads localise in cord structures that become the seminiferous tubules of the testes (Extended Data Fig. 1g). We wondered how PGC clones participate in the different tubules and how they are locally distributed inside the effectively one-dimensional tubules. Second, we aimed to model the dynamics of PGC clones over murine lifetimes, both globally and locally. Together, this extended model provides a quantitative view of the spatial and lifetime dynamics of E6.5 PGC clones.

We continued with PGC clone sizes from the left gonad after the lateral split E9.5

(symmetric to right gonad), as inferred from the embryonic model. Clones were expanded again as a pure birth process to reach ~2000 cells total at E12.5. At E12.5 the expanded clones were then distributed on a one-dimensional spatial lattice, representing the later spatial organisation of postnatal tubules: We introduced two parameters c_1 and c_2 that allow to describe various types of spatial organisation, based on a theory for patch formation (Supplementary Equations c). In short, $c_i \in [0, 1]$ specify the probabilities that the next cell seeded to the spatial lattice is from the same clone as the previous cell. Cells were distributed on a single lattice according to c_1, the lattice split up into 11 different cords, and, lastly, cells were distributed within each cord lattice according to c_2. Hence, c_1 captures clonal aggregation effects in the gonads before cord formation, leading to biased cord participation, while the product $c_1 c_2$ describes the local mixing within a cord after cord compartmentalisation, specifying the patch structure as it develops towards postnatal analysis. As corner cases, this procedure contains fully randomized spatial arrangements ($c_1 = c_2 = 0$), as well as fully aggregated scenarios ($c_1 = c_2 = 1$) where all clones are laid out one after the other.

The developmental expansion from E12.5 to 2 weeks postnatally was modelled as an expanding birth-death process on the spatial tubule lattices. Single cells on the lattice across all cords were expanded with a mean amplification of 30 (from ~2000 PGCs to ~60,000 SSCs per testis[57]) and a single-cell survival chance of 50% (specified by E11.5 barcoding, Extended Data Fig. 6). We factored in the appropriate level of cord-to-cord heterogeneity in this mean expansion (roughly ranging from 20 to 40, Supplementary Equations d, Extended Data Fig. 8d,e). Daughter cells of expanded clones were seeded as immediate neighbours, leading to elongated tubule lattices.

From 2 weeks onwards, clonal dynamics were modelled as a homeostatic process using neighbour competition with an average stem cell replacement time of once every 6 days (following previous studies[37,59]). Concretely, whenever a stem cell differentiated, its empty lattice position was immediately taken by a random left or right neighbour that duplicated in the process. Furthermore, effects of different homeostatic regulations were analysed (see section 'Neighbour and global competition during adult homeostasis').

By using E9.5 clone sizes from the embryonic phase inference and fixing many model parameters as specified above, c_1 and c_2 were the only remaining parameters to be inferred from data. Again, we resorted to simulation-based inference by ABCdeZ.jl. Data of *Polylox* tubule fragments (E6.5&6.75 barcoding, 8- or 9-weeks analysis) were converted to summary statistics of complementary cumulative probability distributions, specifying the fraction of segments

exceeding a certain barcode number (for three different categories of segment lengths and two independent mice; Extended Data Fig. 8a). Starting from flat uniform priors over $[0, 1]$ for c_1 and c_2, analogue model summary statistics were computed iteratively and compared to the data. For the inference, again *Polylox* barcodes were taken as clone sizes. To obtain model summaries, tubules were simulated until 8 weeks postnatally and then cut into fragments matching fragment lengths of the data (using a conversion of ~30 SSCs per mm tubule[57]). Fitting the model to the data yielded a correlated posterior distribution for c_1 and c_2.

To gain the spatial and lifetime dynamics of E6.5 PGC clones, we extrapolated again to the initial ~30 E6.5 PGCs by re-simulating this extended model with c_1 and c_2 samples from their two-dimensional posterior and keeping track of PGC clone identity (instead of *Polylox* barcodes). The model was evaluated at various embryonic and postnatal time points, and local patch sizes as well as global clone sizes (summing all patches of same PGC identity) were inspected.

Neighbour and global competition during adult homeostasis. We investigated the potential advantages of the specific geometry of seminiferous tubules for the lifetime stability of PGC clones. The standard neighbour competition was simulated in one- or quasi-one-dimensional (1D or q-1D) tubular geometries, and compared to a hypothetical reference model with global competition that is agnostic towards geometric dimensionality or form. Simulations showed that the tubular geometries provide superior stability in contrast to the non-geometric reference; a feature that is further supported by Supplementary Equations e and f.

The spatial and lifetime PGC dynamics were re-simulated as before (see section above), until the postnatal homeostatic phase at 2 weeks was reached. From that point onwards, the tubules were simulated in three different ways (Extended Data Fig. 10c). First, as a neighbour competition process on a 1D lattice where left and right neighbours may replace each other (as before, section 'Spatial and lifetime model of PGC clonal dynamics'). Second, as neighbour competition on a q-1D cylindrical lattice, where left/right and below/above neighbours may replace each other. The circumference contained 5 cells with periodic boundaries[37], and hence ~12,000 units in the longitudinal dimension for a total of ~60,000 cells. Third, a reference global competition process, modelled as a critical birth-death process where events of cell division and differentiation balance out on the population average. Clones in the birth-death process develop independently of their neighbours and were assumed to be non-mixing at patch boundaries. All three scenarios were simulated with a stem cell division rate $\lambda = 1/6$ (per day; as before), so that the production of differentiated progeny and sperm are identical.

Simulations tracked E6.5 PGC clones for various time points across the three scenarios. Global clone sizes and local patch sizes were collected to compute end-point-correlations and extinction levels. To quantify the gain of patch stability coming from the inferred average patch size of ~150 cells (Extended Data Fig. 10b), a hypothetical no-patch case was computed by using the single-cell patch extinction probabilities of a 1D neighbour competition model (Extended Data Fig. 10e,h). The single-cell extinction is given by $p(\ell_t = 0) = 1 - e^{-2\lambda t}\big(I_0(2\lambda t) + I_1(2\lambda t)\big)$ (Supplementary Equations e), and hence the extinction chance for a "patch" of ℓ cells, being instead scattered on the lattice, was computed by $p(\ell_t = 0)^{\ell}$. Another set of simulations tracked single cells introduced at E12.5 (PGC sub-clones) in otherwise identical models, to compare clonal diversity over time with the E11.5 barcoding data (Extended Data Fig. 10f). Further, extinction probabilities of single SSC-derived clones (PGC sub-sub-clones) under homeostasis were compared for the 1D neighbour and the global competition model (Extended Data Fig. 10j), setting $\ell_0 = 1$ in Supplementary Equations e.

Finally, the effect of the tubular geometry was analysed in a scenario where a single E6.5 PGC clone had a selective advantage s during the postnatal homeostatic phase. Tubules at 2 weeks were forward simulated with 1D neighbour competition and global competition, increasing the stem cell division rate of the selected clone to $\lambda(1 + s)$ with $s = 1\%$, and reading out the spatial configuration at 2 years postnatally (Extended Data Fig. 10k). The tubular geometry with neighbour competition effectively confined the patches of the "mutated" PGC clone, in contrast to exponentially expanding patches under global competition (Supplementary Equations f).

Temporal transmission bias from fathers to pups. We assessed whether PGC clones have a temporal bias in their contribution to pups over the father's life span. To that end, we computed the times between occurrences of the same barcode and aggregated these inter-birth intervals for all barcodes and the four fathers. A value of zero days corresponds to barcode coincidences in two or more pups on the same day. To obtain a model reference of unbiased barcode transmission, the barcodes were randomly shuffled across the pups of a given father and inter-birth intervals were recomputed as done for the data. The data distribution of inter-birth intervals was compared to the unbiased model based on repeated simulations providing median and 95% credible intervals (Extended Data Fig. 3g). Further, the data was reduced to barcodes with a maximum barcode frequency of 10%, 5% or 2% and simulations of the unbiased model were recomputed to obtain right-tailed *p*-values under a null distribution for clonal coincidences[60] (Extended Data Fig. 3h).

2. Supplementary Equations (a, b, c, d, e and f)

a, Rescaled clone size distributions of single PGCs. Analysis of rescaled clone size distributions (as done in Extended Data Fig. 4a,b) shows that clonal dynamics of PGCs conform with a neutral birth-death process. Due to this observation, we implemented the models for the barcoding data based on these stochastic processes (dynamics from E6.5 to E12.5, Fig. 3, and also extended from E6.5 to 2 weeks, Fig. 5). The clone sizes from E6.5 barcoding reveal the nature of the clonal dynamics in the expanding embryonic phase. The scaling law then applies even for adult analysis stages, as clones stabilise before entering the adult homeostatic phase (compare with Fig. 3) and continued turnover is neutral among surviving clones (see also Supplementary Equations b, Extended Data Fig. 4c,d). We briefly outline the well-known theory of birth-death processes, to state the scaling law that we applied to the barcoding data.

In birth-death processes, two types of transitions are possible: An individual cell may divide with chance $\lambda(t)\mathrm{d}t$ ("birth") and leave the compartment of interest with chance $\mu(t)\mathrm{d}t$ ("death") in any short time span $\mathrm{d}t$. The division and loss rates, $\lambda(t)$ and $\mu(t)$, are the same for all cells in the considered compartment. Particularly, they are independent of the clone identity and current clone size, and as such the process is neutral. The rates may however vary as a function of time t; this includes our models with sequential phases. For this process, the probability distribution of clone sizes $X_t = x$ at time t for any initial clone size $X_0 = x_0$ are available (simple non-homogenous birth-death process; Bailey, 1964[61]). Focusing on clones derived from single cells, $x_0 = 1$, the distribution is given by $p(x) = (1-\alpha)\,(1-\beta)\,\beta^{x-1}$ (for $x \geq 1$) and $p(0) = \alpha$, where $\alpha = 1 - 1/\left(e^{\rho(t)} + A(t)\right)$ and $\beta = 1 - e^{\rho(t)}/\left(e^{\rho(t)} + A(t)\right)$ with $\rho(t) = \int_0^t \{\mu(\tau) - \lambda(\tau)\}\mathrm{d}\tau$ and $A(t) = \int_0^t \lambda(\tau) e^{\rho(\tau)}\mathrm{d}\tau$. The solution includes the time-homogenous processes (critical, sub- and supercritical). For *Polylox* data it is natural to condition this distribution on survival (as we can only observe extant clones that did not go extinct before analysis). Under this condition, $X_t \geq 1$, the distribution simplifies to a shifted Geometric distribution with $p(x) = (1-\beta)\,\beta^{x-1}$, where $x \in \{1, 2, \ldots\}$, and mean clone size $\mathbb{E}(X_t) = 1/(1-\beta)$. So, while considering a broad class of processes, all clone sizes fall on the same distributional shape with only one effective parameter—its mean clone size.

Thus, we rescale the extant clones with their mean. We consider $W_t = X_t/\mathbb{E}(X_t)$ and obtain $p(W_t > w) = \beta^{\lfloor w/(1-\beta) \rfloor}$, with floor function $\lfloor\,\rfloor$. Further, in the continuous limit for expanded clones ($\beta \to 1$, $w > 0$), rescaled clone sizes simplify to $p(W_t > w) = e^{-w}$. Both expressions were used (Extended Data Fig. 4a,b) and pose a simple but strong test of neutrality

and compatibility with the class of birth-death processes.

Of note, other neutral processes (e.g., homeostatic Moran process without selection) can settle on the same scaling law[62]. We further note that non-simultaneous introduction of clonal barcodes *in vivo* should not be a problem for the scaling analysis: Clonal barcodes in model simulations (being created over a 1.5-day recombination window) still scale (Extended Data Fig. 5d), showing that this effect does not distort clone sizes significantly in our system. Lastly, the random split of clone sizes (binomial sampling) into left and right gonad is allowed within the above birth-death processes. Binomial sampling is mathematically equivalent to a pure death process, and hence the stated distributions and scaling laws remain unchanged.

b, Theory of inherent and persistent clonal bias. In the following we derive a theory to investigate whether, and to which degree, clone sizes that conform with the neutral scaling law (Supplementary Equations a) actually indicate an underlying neutral mechanism. To that end, clonal dynamics are considered where some clones exhibit inherent and persistent selective advantages, termed "clonal bias", deviating from purely neutral behaviour. We find a criterion that directly links non-neutral clone sizes to the fractions of clone size variability that are caused by clonal bias and neutral stochasticity, respectively. This theory confirms that the principal source underlying the observed germline clone size variation is neutral stochasticity (85% - 100%).

Following up on Supplementary Equations a, we start by considering single-cell derived, extant clones driven by birth-death dynamics. Under neutral clonal behaviour, clone sizes $X = x$ at analysis follow the distribution $p(x) = (1-\beta)\,\beta^{x-1}$, $x \in \{1, 2, \dots\}$, where β, and hence the mean clone size $\mathbb{E}(X) = 1/(1-\beta)$, is identical for all clones. To introduce systematic clonal bias and selective advantages, we now lift this assumption and allow for clone-specific dynamics and mean sizes. Concretely, a random variable g, the clone-specific mean clone size, is introduced such that $\mathbb{E}(X \mid g) = 1/\big(1-\beta(g)\big) \equiv g$ for individual clones. This means that each individual clone evolves according to division and loss rates identical across all its constituent cells; however, these rates may vary across cells of different clones. To parametrize g on the mean and variance level, we set $\mathbb{E}(g) = \mu$ and $\mathrm{Var}(g) = \sigma^2$. The neutral case is then contained with $\sigma = 0$, while $\sigma > 0$ implies that some clones will obtain a selective advantage (for events $g > \mu$) and others are disadvantaged ($g < \mu$). The mean observed clone size across all (potentially biased) clones is calculated to $\mathbb{E}(X) = \mu$, independent of neutral or non-neutral dynamics. In contrast, the variance across all clones is given by $\mathrm{Var}(X) = (\mu-1)\mu + 2\sigma^2$ leading to a

coefficient of variation (CV) of $\mathrm{CV}(X) = \sqrt{\mathrm{Var}(X)}/\mathbb{E}(X) = \sqrt{1 - 1/\mu + (2\sigma^2)/(\mu^2)}$. Here, while neutral dynamics approach a maximal CV of one, non-neutral dynamics can generate clone size variation beyond this limit.

To obtain a "scale-free" view on clone size variability, i.e. independent of the mean clone size μ, we introduce a dimensionless bias parameter b that quantifies the excess of non-neutral clone size variation beyond the neutral baseline. Concretely, we set $\mathrm{CV}(X) = (1 + b)\sqrt{1 - 1/\mu}$, where $b \geq 0$ and $\sqrt{1 - 1/\mu}$ is the CV of the neutral case ($\sigma = 0$). From this, one obtains the conversion $\sigma = \sqrt{(1/2)\, b(b + 2)\, (\mu - 1)\mu}$. Such clonal bias, quantified via b, allows to directly compare the shapes of scale-free clone size distributions (i.e., rescaled) for neutral ($b = 0$) and various non-neutral clonal dynamics ($b > 0$), as done in Extended Data Fig. 4c ($b \in \{0.0, 0.05, 0.2, 0.5, 1.0\}$). To visualize concrete distributions, g was sampled from a shifted gamma distribution, setting $g \sim \mathrm{Gamma}(\alpha, \theta) + 1$ (with shape α and scale θ) and $\alpha = ((\mu - 1)/\sigma)^2$ and $\theta = (\mu - 1)/\alpha$, where σ was specified by the above conversion from b and μ. Then $\mathbb{E}(g) = \mu$ and $\mathrm{Var}(g) = \sigma^2$ as desired.

It remains to be investigated to what extent inherent clonal bias (or selective advantages) actually causally contributes to the observed variation of clone sizes (the shapes of these rescaled distributions). For this, the observed extant clone sizes, X, are correlated with their inherently biased means, g. If initial biases among clones faithfully predict and determine later "winner" and "loser" clones (i.e., big and small clones), this equates to a high correlation. In contrast, a low correlation reveals that—even if biases among clones may exist—neutral stochasticity dominates effects of clonal bias so that the "winner" and "loser" clones are simply determined by chance. In this sense, the squared Pearson correlation $r^2(X, g)$ determines the fraction of the clone size variance that is explained by clonal bias ($\mathrm{Var}(X)$ explained by g) and is computed subsequently. First, the joint expectation can be derived to $\mathbb{E}(Xg) = \mathbb{E}(g^2) = \mu^2 + \sigma^2$. Then, it follows that $r^2 = \mathrm{cor}(X, g)^2 = \mathrm{Var}(g)/\mathrm{Var}(X) = \sigma^2/\big((\mu - 1)\mu + 2\sigma^2\big)$. Finally, by using the above conversion to express σ in terms of the clonal bias b and mean clone size μ, one obtains the result $r^2(X, g) = (1/2)\,\big(b(b + 2)\big)/\big(1 + b(b + 2)\big)$, which becomes independent of μ. Hence, shapes of the rescaled clone size distributions, as set by the clonal biases b, directly relate to the fraction of clone size variability, r^2, attributable to inherent and persistent selective advantages. The remaining fraction, $1 - r^2$, is hence the clone size variability explained by neutral stochasticity. This result provides a simple yet powerful criterion to assess the contributions of neutral vs. selective clonal dynamics directly from the observed variation of clone sizes.

Comparing the theoretical clone size distributions (Extended Data Fig. 4c) to the experimental distributions (Extended Data Fig. 4a,b) reveals no skewness in the data as it would be expected from inherent clonal bias. Additionally, already a bias of 20% ($b = 0.2$) deviates noticeably from the neutral distribution (Extended Data Fig. 4c), and, as such, may be considered the maximal clonal bias hidden in the data. This extent of clonal bias corresponds to a causal contribution of 15%, at maximum, to the observed clone size variability; conversely, at least, 85% of the variability is caused by neutral stochasticity (Extended Data Fig. 4d). Together, these results show that clonal dynamics that appear neutral also indicate an underlying neutral mechanism. The neutral clone sizes of the germline hence pose a strict restriction to the level of inherent and persistent selective advantages among PGC clones. If inherent clonal biases exist at all, they must be either rather transient or mild in effect.

c, Theory of patch formation. We derive a theory for the patches that a clone forms when being distributed on a one-dimensional spatial lattice, representing the forming cords in the embryo and the later tubules in postnatal testes. Patch formation is described by a local correlate of how much a clone identity of a cell predicts the clone identity of its neighbouring cells. Concretely, we introduce a probability $c \in [0, 1]$ that the next cell on the lattice, viewed from left to right, is occupied by a cell of the same clone. This principle, starting from a patch with its first cell, induces patch lengths (or sizes) $\ell \in \{1,2, \dots\}$ that follow a shifted geometric distribution ($\ell - 1$ "successes", i.e. further cells of the same clone, before the first "failure") with probabilities $p(\ell) = (1 - c)\, c^{\ell-1}$. However, for a clone of N cells total, a patch length has to be bounded by $\ell \leq N$, and the fragmentation of the clone leads to $n \in \{1, \dots, N\}$ distinct patches of sizes ℓ_i, such that $\sum_{i=1}^{n} \ell_i = N$. Hence, we aim to derive, conditioned on the clone size N and c given, the distribution of the number of patches $p(n|N)$ and the distribution of patch lengths $p(\ell_i|n, N)$ for each patch i.

To compute $p(n|N)$ one notes that the inverted probability $p(N|n)$ is given by a shifted negative binomial distribution, as the sum of independently formed patches that are geometrically distributed with $p(\ell_i)$. We have $N|n \sim \mathrm{NegBin}(n, 1 - c) + n$ with probabilities $p(N|n) = p(\sum_{i=1}^{n} \ell_i\, |n) = \binom{N-1}{n-1} c^{N-n}\, (1 - c)^n$. Then Bayes theorem allows the conversion to $p(n|N)$. With an uninformed prior for the number of patches, $p(n) = 1/N$, one obtains $p(n|N) = \binom{N-1}{n-1} c^{N-n}\, (1 - c)^{n-1}$. Thus, the number of patches follows a modified binomial distribution, $n|N \sim \mathrm{Bin}(N - 1, 1 - c) + 1$, with a mean patch number $\mathbb{E}(n|N) = (N - 1)(1 - c) + 1$, and noteworthy corner cases of a single patch containing all N cells at once ($n = 1$ if $c = 1$) vs. N

single-cell patches ($n = N$ if $c = 0$).

Given c and clone size N, and with that also the patch number n from above, the distribution of patch sizes $p(\ell_i|n, N)$ is obtained in iterative manner. We introduce ℓ_1, the size of the first patch and, stochastically independent, $\ell_{-1} = \sum_{i=2}^{n} \ell_i$, the combined sizes of the patches after the first. It follows $p(\ell_1 = x|n, N) = p(\ell_1 = x)\, p(\ell_{-1} = N - x)/p(\ell_1 + \ell_{-1} = N)$ (where the right-hand side probabilities are shifted negative binomial distributions from above), leading to $p(\ell_1|n, N) = \binom{N-1-\ell_1}{n-2}/\binom{N-1}{n-1}$, with patch sizes in the range $1 \leq \ell_1 \leq N - n + 1$. Further, we derive that all subsequent patch sizes can be obtained iteratively: The patch size ℓ_i is given by the same distribution, only by updating $N_{new} = N - \ell_{i-1}$ and $n_{new} = n - 1$; for example, the second patch length is given by $p(\ell_2|\ell_1, n, N) = \binom{N-\ell_1-1-\ell_2}{n-3}/\binom{N-\ell_1-1}{n-2}$. We implemented an algorithm to robustly evaluate the involved ratio of binomial coefficients, termed the $\mathrm{BinRatio}(n, N)$ distribution in code. The mean value of this distribution is $\mathbb{E}(\ell|n, N) = N/n$, while the mean patch length over all (random) patch numbers n is computed to $\mathbb{E}(\ell|N) = (1 - c^N)/(1 - c)$.

Of note, this theory is closed under repeated patch formations: Fragmenting a clone of N cells with $c_1 \in [0,1]$ and fragmenting the resulting patches (viewing patch lengths as clone sizes ℓ_i) another time with $c_2 \in [0,1]$, is identical to a single fragmentation using the product value $c = c_1 c_2$ on the initial clone size N directly. This indicates that complex biological fragmentation processes may be well-captured descriptively by a single or few parameters, correlating clone identities of cell neighbours.

Combining above derivations, a list of patch sizes can be generated over all clones, by first sampling the number of patches for a given clone and then sampling the size of each patch iteratively. In summary, this theory provides a full stochastic framework to spatially distribute clones with given clone sizes on a one-dimensional lattice, encapsulated in a single parameter c that specifies the statistics of the number and lengths of the formed patches.

d, Theory of foetal patch elongation dynamics. We develop a model for the dynamics of patch sizes inside the expanding tubules, spanning from cord formation (E12.5) to the postnatal tubules (2 weeks) at which the homeostatic phase is entered. The model accounts for growth differences in the cords (that is, some cords elongate to long tubules in the adult, some to short), at a magnitude that we validate through independent features in the barcoding data.

Each gonad (the later testis) forms ~11 cords (the later tubules) that roughly expand from 2,000 PGCs at E12.5 to 60,000 SSCs at two weeks after birth (and thereafter), meaning that

PGCs amplify 30-fold on average. We compare the coefficient of variation (CV) at these two time points, to assess to what extent PGC expansion is heterogeneous across different cords. Embryonic cord cell numbers have a $\mathrm{CV}_{\mathrm{E12.5/E13.5}} \approx 0.31$ (Extended Data Fig. 1g and 8d), that increases to $\mathrm{CV}_{\mathrm{adult}} \approx 0.43$ (Nakata et al., 2015[38]; where tubule T6 was excluded as a likely merger two cords; Extended Data Fig. 8d). Subsequently a theory is derived to show that this increase in variation cannot be explained by homogenous stochasticity of PGC expansion but warrants systematic growth differences between elongating tubules.

We assume that a cord i has X_i cells initially (E12.5), elongating to Y_i cells postnatally. Within a given cord, single PGCs follow an expanding (supercritical) birth-death process, captured in the random variables Z_{ij}, such that the sum of all single PGC expansions generates the elongated tubule, i.e. we have $Y_i = \sum_{j=1}^{X_i} Z_{ij}$. We inform single-cell expansions by the mean $\mathbb{E}(Z_{ij}) = \mu = 30$ (from 2,000 to 60,000, over all cords), and survival chance $p(Z_{ij} \geq 1) = 1 - a = 50\%$ (E11.5 barcoding, Extended Data Fig. 6). To probe heterogeneity between single-cell expansions across cords, we allow that $\mathbb{E}(Z_{ij}|i) = g_i$, where g_i is a (random) per-cord expansion; all cells of the same cord amplify with same mean g_i, but cells of different cords may be subject to varying mean expansions. Then, it follows that $\mathbb{E}(g_i) = \mu$ is specified, while $\mathrm{Var}(g_i) = \sigma^2$ expresses the level of cord expansion variation through the additional parameter σ. The homogeneous case is contained with $\sigma = 0$, and $\sigma \gg 0$ encodes heterogeneous expansion. Critically, this framework enables the derivation of means and variances of all involved quantities. We obtain the mean relation $\mathbb{E}(Y_i) = \mu\, \mathbb{E}(X_i)$ and a variance of tubule cells after elongation as

$$\mathrm{Var}(Y_i) = \mathbb{E}(X_i) \frac{\mu\,(a-1) + (\mu^2 + \sigma^2)\,(a+1)}{1-a} + \mathbb{E}(X_i)^2\,\sigma^2 + (\mu^2 + \sigma^2)\,\mathrm{Var}(X_i).$$

Hence, σ can be computed directly from the embryonic and adult CVs using

$$\sigma^2 = \frac{\mu\,(1 - a + \mu\,((1-a)\,(\mathrm{CV}(Y_i) - \mathrm{CV}(X_i))\,(\mathrm{CV}(X_i) + \mathrm{CV}(Y_i))\,\mathbb{E}(X_i) - (1+a)))}{1 + a + (1-a)\,(1 + \mathrm{CV}(X_i)^2)\,\mathbb{E}(X_i)}.$$

When inserting values of $\mu = 30$, $a = 0.5$, $\mathbb{E}(X_i) = 2000/11$, $\mathrm{CV}(X_i) = \mathrm{CV}_{\mathrm{E12.5/E13.5}} \approx 0.31$ and $\mathrm{CV}(Y_i) = \mathrm{CV}_{\mathrm{adult}} \approx 0.43$, we obtain $\sigma \approx 7.5$. This indicates substantial variation in cord expansion, with some cords expanding 20-fold, and others 40-fold, to have on average a 30-fold increase in cell numbers. In simulations, we parametrize the mean cord expansion by $g_i \sim \mathrm{Gamma}(\alpha, \theta) + 1$ (with shape α and scale θ) and set $\alpha = ((\mu - 1)/\sigma)^2$ and $\theta = (\mu - 1)/\alpha$, satisfying $\mathbb{E}(g_i) = \mu$ and $\mathrm{Var}(g_i) = \sigma^2$ as desired (Extended Data Fig. 8d, for an overall scheme). Thus, solely by comparing cell number variation in embryo and adult, we can specify a model for the expansion of the testis cords becoming elongated tubules at appropriate

mean and variance levels.

As the barcoding data is not being used to set up the expansion model or specify σ, we wondered if a feature in that data allows to test the model. If the substantial heterogeneity in the effectively one-dimensional elongations were true, one would expect the following: On average, the barcode patches, created at cord formation, are more stretched out in longer tubules at their final length, while in less elongated tubules barcodes are compressed in a shorter length. Hence, we compared the mean barcode number in small fragments (that came preferentially from shorter tubules) vs. the mean barcode number in sub-fragments that are pieces of a long fragment (preferentially a long tubule); where both were subsampled to an identical fragment length distribution. Indeed, we observe a slight shift between these mean values in both mice (~0.3 barcodes in mouse 2), while (without fitting these data) the model predicts a similar shift (~0.2 for mouse 2; Extended Data Fig. 8e); in contrast, no shifts (for $\sigma = 0$) or drastic shifts of more than one barcode ($\sigma \gg 7.5$) are possible. This independent feature in the barcoding data validates the determined level of cord variation of the expansion model with $\sigma \approx 7.5$.

e, Theory of patch length variation in adult homeostasis. We develop a theoretical view of the patch length variation that explains the increased stability of patches in the neighbour competition model (tubular geometry) compared to the global competition model (agnostic of spatial geometry). To that end we derive the time evolution of the coefficient of variation (CV, standard deviation divided by the mean) for typical patch lengths in both models.

In the global competition model birth (cell division) and death (here representing biological cell differentiation) events of stem cells are balanced out, on average, on the population level. As a model we used the critical birth-death process, with a birth rate λ equaling the death rate. The mean and variance of patch sizes ℓ_t over time t, starting with an initial size of $\ell_0 \geq 1$ cells, are known to be $\mathbb{E}(\ell_t) = \ell_0$ and $\mathrm{Var}(\ell_t) = 2\ell_0\lambda t$ (Bailey, 1964[61], Equations 8.54, 8.55, 8.58; Supplementary Equations a) with a probability of extinction as $p(\ell_t = 0) = (\lambda t/(1+\lambda t))^{\ell_0}$. Hence, patch lengths under global competition vary as $\mathrm{CV}_{\mathrm{global}}(\ell_t) = \sqrt{2\lambda t/\ell_0}$.

In the neighbour competition model stem cell differentiation is compensated by the immediate division of neighbouring cell (semantically equivalent to a replacement of a cell by one of its neighbours). The model achieves the same differentiation output as the global competition model when such replacements happen with the same rate λ. Importantly, a patch of cells with the same clone identity maintains an unaltered size if replacements take place within

the patch boundaries (cells replacing cells of same clone identity). Hence the evolution of the patch length is only driven by the stem cell dynamics at the patch boundaries. On a one-dimensional lattice, we observe shifts of the left boundary with a rate λ, as the patch increases by one cell when its leftmost cell replaces its left neighbour (rate $\frac{\lambda}{2}$), and the patch shrinks by one when its leftmost cell is replaced by its left neighbour of a different clone identity (rate $\frac{\lambda}{2}$). With analogue dynamics at the right boundary, we obtain a total rate of 2λ, independent of the current patch length ℓ_t. Hence one realizes that the patch length ℓ_t is described by a time-continuous symmetric random walk with an absorbing state at $\ell = 0$ for patch extinction. The solution of this process is known as $p(\ell_t = \ell) = e^{-2\lambda t}\left(I_{\ell-\ell_0}(2\lambda t) - I_{\ell+\ell_0}(2\lambda t)\right)$ (for $\ell \geq 1$) and $p(\ell_t = 0) = 1 - e^{-2\lambda t}\sum_{\ell=1}^{2\ell_0} I_{\ell-\ell_0}(2\lambda t)$, where $I_\nu(x)$ is the modified Bessel function of first kind and ℓ_0 is the patch length at time $t = 0$ (Heathcote and Moyal, 1959[63]). The mean follows as $\mathbb{E}(\ell_t) = \ell_0$ (identical to a random walk without absorbing state). The variance is given by $\mathrm{Var}(\ell_t) \approx 2\lambda t$ for our typical parameter regime (low probabilities of patch extinction for neighbour regulation, see below). This implies that patch lengths under local neighbour competition vary as $\mathrm{CV}_{\mathrm{neighbour}}(\ell_t) \approx \sqrt{2\lambda t}/\ell_0$.

Critically, the variance under neighbour competition does not scale with the initial patch size, in contrast to the linear dependence under global competition. For typical parameters of $t = 365$ days, $\lambda = 1/(6\text{ days})$ and our inferred mean patch size of $\ell_0 \approx 150$ cells (Extended Data Fig. 10b), we obtain patch extinction probabilities as $p(\ell_t = 0) \approx 0.087$ (global) and $p(\ell_t = 0) \approx 1.9 \times 10^{-38}$ (neighbour); and hence, $\mathrm{CV}_{\mathrm{global}} \approx 0.90$ and $\mathrm{CV}_{\mathrm{neighbour}} \approx 0.07$. This explains the drastic differences in long-term patch stability between the two competition models. Of note, we may extrapolate to a human testis by estimating the size of adult patches that reach a similar stability over a comparable human life span. Assuming the same division rate of individual stem cells and considering $t = 50$ years, a CV of 7% is reached at $\ell_0 \approx 1050$, suggesting a seven times larger human stem cell pool of about 420,000 cells per testis.

f, Effect of tubular geometry under selection. We investigate the effect of the tubular geometry by equipping a single PGC clone with a selective advantage $s > 0$ during the postnatal homeostatic phase. This selective advantage may originate from a mutation or epigenetic modification that was acquired during development, and enhances stem cell division in all tubular patches of the selected clone in the adult. The selected clone competes with neutral PGC clones within the testis which follow the dynamics as described in Supplementary Equations e.

Under global competition, the selected clone divides with an increased rate $\lambda(1 + s)$

per cell; hence, its individual patches expand with a mean of $\mathbb{E}(\ell_t) = \ell_0 e^{\lambda s t}$, where ℓ_0 is the patch size at 2 weeks postnatally. Under neighbour competition (in 1D), the selected clone has an increased stem cell replacement rate of $\lambda(1+s)$. Here, in contrast, the selective advantage is neutralised within each patch, as all neighbouring cells share the same advantage. A patch of the selected clone realises its advantage only at the patch boundaries, gaining cells with a constant rate of $\lambda(1+s)$ per patch, while losing cells with rate λ. Hence, patches of the selected clone expand as an asymmetric random walk[63] with a mean of $\mathbb{E}(\ell_t) \approx \ell_0 + \lambda s t$, under negligible patch extinction (Supplementary Equations e).

With a selective advantage of $s = 2\%$, a neutral division rate of $\lambda = 1/(6\text{ days})$ and a time span from 2 weeks to 2 years postnatally, a patch of $\ell_0 = 150$ cells expands to only ~152 cells on average under neighbour competition, while the patch would amplify >10-fold under global competition, reaching an average size of ~1632 cells. Thus, neighbour competition within the tubular testis geometry effectively confines selected clones to a slow linear expansion, in contrast to a fast exponential expansion in the hypothetical non-geometric environment.